

# Suppressed heat conductivity in the intracluster medium: implications for the magneto-thermal instability

Thomas Berlok<sup>1,2\*</sup>, Eliot Quataert<sup>3,4</sup>, Martin E. Pessah<sup>2</sup> and Christoph Pfrommer<sup>1</sup>

<sup>1</sup>Leibniz-Institut für Astrophysik Potsdam (AIP), An der Sternwarte 16, D-14482 Potsdam, Germany

<sup>2</sup>Niels Bohr International Academy, Niels Bohr Institute, Blegdamsvej 17, DK-2100 Copenhagen Ø, Denmark

<sup>3</sup>Department of Astrophysical Sciences, Princeton University, Princeton, NJ 08544, USA

<sup>4</sup>Department of Astronomy and Theoretical Astrophysics Center, University of California, Berkeley, CA 94720-3411, USA

Accepted XXX. Received YYY; in original form ZZZ

## ABSTRACT

In the outskirts of the intracluster medium (ICM) in galaxy clusters, the temperature decreases with radius. Due to the weakly collisional nature of the plasma, these regions are susceptible to the magneto-thermal instability (MTI), which can sustain turbulence and provide turbulent pressure support in the ICM. This instability arises due to heat conduction directed along the magnetic field, with a heat conductivity which is normally assumed to be given by the Spitzer value. Recent numerical studies of the ion mirror and the electron whistler instability using particle-in-cell codes have shown that microscale instabilities can lead to a reduced value for the heat conductivity in the ICM. This could in turn influence the efficiency with which the MTI drives turbulence. In this paper we investigate the influence of reduced heat transport on the nonlinear evolution of the MTI. We study plane-parallel, initially static atmospheres and employ a subgrid model that mimics the influence of the mirror instability on the heat conductivity. We use this subgrid model to assess the effect of microscales on the large scale dynamics of the ICM. We find that the nonlinear saturation of the MTI is surprisingly robust in our simulations. Over a factor of  $\sim 10^3$  in the thermal-to-magnetic pressure ratio and collisionality we find at most modest changes to the saturation of the MTI with respect to reference simulations where heat transport is unsuppressed.

**Key words:** galaxies: clusters: intracluster medium – conduction – diffusion – plasmas – instabilities – magnetic fields.

## 1 INTRODUCTION

The intracluster medium of galaxy clusters consists of a plasma with high temperature ( $T \sim 10^7$ – $10^8$  K) and low number density ( $n \sim 10^{-4}$ – $10^{-2}$  cm<sup>-3</sup>). This plasma is weakly collisional and has, as a result, convective stability properties that differ from those expected from the Schwarzschild criterion (Schwarzschild 1958). The new stability properties arise as a consequence of anisotropic transport of heat, in which the heat flow is directed along the local magnetic field. The physics of this anisotropic transport has been modelled using Braginskii MHD (Braginskii 1965) in which the heat flow vector,  $\mathbf{Q}$ , is given by

$$\mathbf{Q} = -\chi_{\parallel} \mathbf{b} \mathbf{b} \cdot \nabla T, \quad (1)$$

where  $\chi_{\parallel}$  is the heat conductivity (Spitzer 1962),  $\mathbf{b}$  is a unit vector directed along the magnetic field,  $\mathbf{b} \mathbf{b}$  is a dyadic product, and  $T$  is the temperature of the plasma.

Two of the widely studied instabilities that arise due to anisotropic transport of heat are the magneto-thermal instability

(MTI, Balbus 2000, 2001) and the heat-flux-driven buoyancy instability (HBI, Quataert 2008). The MTI can be active for stratified atmospheres in which the temperature decreases with height and has been studied using Braginskii MHD (Parrish & Stone 2005; Parrish et al. 2008; Kunz 2011; Kunz et al. 2012; Parrish et al. 2012a,b).

While Braginskii MHD can describe some features of weakly collisional systems it does not correctly describe all the microscale instabilities that a weakly collisional plasma such as the ICM can support (Schekochihin et al. 2005; Schekochihin & Cowley 2006). In fact, fully collisionless plasmas are better described by the Vlasov-Maxwell equations (Ichimaru 1973; Krall & Trivelpiece 1973; Swanson 1989; Stix 1992). This system of equations can be used to derive the linear theory of kinetic instabilities such as the mirror and firehose instabilities (Chandrasekhar et al. 1958; Parker 1958; Hasegawa 1969; Gary 1993) which are driven by anisotropy in velocity space with respect to the magnetic field. The nonlinear evolution of these microscale instabilities can be studied by employing particle-in-cell simulations (PIC, Hockney & Eastwood 1988; Birdsall & Langdon 1991).

Studies of velocity-space instabilities in collisionless plasmas

\* E-mail: tberlok@aip.de

have shown that the effective heat conductivity can be reduced by the ion mirror instability (Komarov et al. 2016; Riquelme et al. 2016) and the electron whistler instability (Roberg-Clark et al. 2016; Riquelme et al. 2016; Roberg-Clark et al. 2018a,b; Komarov et al. 2018). This suppression of heat conductivity could potentially influence the evolution and saturation of the MTI and the HBI which both have growth rates that depend on the magnitude of the anisotropic heat conductivity,  $\chi_{\parallel}$ . We focus in the following on the MTI because it is expected to be active in the outskirts of clusters where the plasma- $\beta$  is higher and the collisionality is lower than in the inner regions of the cluster. Both a weak magnetic field and a low collisionality conspire to make a plasma prone to the mirror instability and it seems likely that their presence can influence the dynamics of the ICM in this region.

While PIC simulations of the Vlasov-Maxwell systems can be used to study small-scale instabilities in the ICM they are so far too computationally expensive to be used for studies of the large scale dynamics. In this paper we instead attempt to bridge the two approaches (PIC and Braginskii-MHD) by using published PIC simulations to motivate a subgrid model for the heat conductivity in the ICM. We use this subgrid model for the heat conductivity in simulations of the MTI in order to assess whether the microscale instabilities modify its evolution.

Our study is performed using a plane-parallel approximation to the ICM atmosphere which we assume to be initially in hydrostatic equilibrium. We are thus neglecting the effects of turbulence driven by e.g. AGN or mergers (Zuhone et al. 2011; McNamara & Nulsen 2012; Kannan et al. 2017; Barnes et al. 2019). Such external turbulence can modify the MTI directly by randomizing field lines (McCourt et al. 2011; Ruszkowski et al. 2011) and/or indirectly by increasing the volume fraction of the ICM which is mirror unstable (e.g. Santos-Lima et al. 2014) and has a lower heat conductivity. This interaction between AGN/merger driven turbulence and MTI depends on the details of the turbulence (e.g. its strength and injection scale relative to the atmosphere scale height, see McCourt et al. 2011) and is likely to have a time-dependent character since the AGN/merger driving changes in time. In this paper we only provide a qualitative discussion of external turbulence as a detailed understanding of this interaction requires dedicated cosmological simulations.

The rest of the paper is outlined as follows. In Section 2, we introduce the equations of Braginskii-MHD along with subgrid models for viscosity (Section 2.3) and heat conduction (Section 2.4). In Section 3, we then study how the MTI is modified by suppression of heat conduction in mirror unstable regions. We present our numerical setup (Section 3.1), expectations from local linear theory (Section 3.2) and a simulation of the interruption of a single eigenmode of the MTI (Section 3.3). We analyze a 2D nonlinear MTI simulation (Section 3.4), perform a parameter study (Section 3.5), and compare our 2D findings with 3D simulations (Section 3.6). We summarize and discuss our results and its limitations (e.g. the role of external turbulence and other plasma instabilities) in Section 4. The appendices include additional details on how sound waves are modified by our subgrid model for heat conductivity (Appendix A), the quasi-global linear theory for the MTI (Appendix B) and a resolution study of our simulations (Appendix C).

## 2 FLUID DESCRIPTION OF WEAKLY COLLISIONAL PLASMAS - EQUATIONS AND SUBGRID MODELS

### 2.1 Equations of Braginskii-MHD

In Braginskii-MHD, the mass continuity equation, the momentum equation, the induction equation, and the energy equation are given by (Braginskii 1965; Kulsrud 1983; Schekochihin et al. 2010)

$$\frac{\partial \rho}{\partial t} + \nabla \cdot (\rho \mathbf{v}) = 0, \quad (2)$$

$$\frac{\partial (\rho \mathbf{v})}{\partial t} + \nabla \cdot \left( \rho \mathbf{v} \mathbf{v} + p_{\text{T}} \mathbf{1} - \frac{B^2}{4\pi} \mathbf{b} \mathbf{b} \right) = -\nabla \cdot \mathbf{\Pi} + \rho \mathbf{g}, \quad (3)$$

$$\frac{\partial \mathbf{B}}{\partial t} = \nabla \times (\mathbf{v} \times \mathbf{B}), \quad (4)$$

$$\frac{\partial E}{\partial t} + \nabla \cdot \left[ (E + p_{\text{T}}) \mathbf{v} - \frac{\mathbf{B}(\mathbf{B} \cdot \mathbf{v})}{4\pi} \right] = -\nabla \cdot \mathbf{Q} - \nabla \cdot (\mathbf{\Pi} \cdot \mathbf{v}) + \rho \mathbf{g} \cdot \mathbf{v}, \quad (5)$$

where  $\rho$  is the mass density,  $\mathbf{v}$  is the fluid velocity,  $\mathbf{B}$  is the magnetic field with direction  $\mathbf{b}$  and  $p_{\text{T}} = p + B^2/8\pi$  is the total (gas plus magnetic) pressure. Here the total energy density is

$$E = \frac{1}{2} \rho v^2 + \frac{B^2}{8\pi} + \frac{p}{\gamma - 1}, \quad (6)$$

with  $\gamma = 5/3$  and  $p = \rho k_{\text{B}} T / m_{\text{H}} \mu$  where  $k_{\text{B}}$  is Boltzmann's constant,  $m_{\text{H}}$  is the proton mass and  $\mu$  is the mean molecular weight. Gravity is included in the momentum and energy equations. In our numerical models we will take the gravitational acceleration to be  $\mathbf{g} = -g \mathbf{e}_z$  where  $g$  is a constant.

The equations of Braginskii-MHD, equations (2)-(5), differ from ideal MHD by the inclusion of two diffusive effects, anisotropic heat conduction and viscosity (the latter known as Braginskii viscosity). The anisotropic heat flux,  $\mathbf{Q}$ , is present in the energy equation, equation (5), and has already been introduced in equation (1). It describes electron heat conduction which is directed along the direction of the magnetic field. Its magnitude depends on the heat conductivity,  $\chi_{\parallel}$ , which is related to the heat diffusivity by  $\kappa_{\parallel} = \chi_{\parallel} T / p$ .

The anisotropic viscosity tensor,  $\mathbf{\Pi}$ , enters in both the momentum and energy equations, and is given by

$$\mathbf{\Pi} = -\Delta p \left( \mathbf{b} \mathbf{b} - \frac{1}{3} \mathbf{1} \right), \quad (7)$$

where  $\Delta p = p_{\perp} - p_{\parallel}$  is the pressure anisotropy and  $p_{\parallel}$  ( $p_{\perp}$ ) is the pressure parallel (perpendicular) to the magnetic field. In a weakly collisional plasma, the pressure anisotropy can be assumed to be given by (Schekochihin et al. 2005)

$$\Delta p = \rho \nu_{\parallel} \frac{d \ln B^3 \rho^{-2}}{dt} = \rho \nu_{\parallel} (3 \mathbf{b} \mathbf{b} : \nabla \mathbf{v} - \nabla \cdot \mathbf{v}), \quad (8)$$

where  $\nu_{\parallel}$  is the viscosity coefficient and  $d/dt = \partial/\partial t + \mathbf{v} \cdot \nabla$  is the Lagrangian derivative.

### 2.2 Transport coefficients

The values of  $\nu_{\parallel}$  and  $\chi_{\parallel}$  are set by the collisionality of the plasma. In standard Braginskii-MHD, these are

$$\chi_{\parallel} = \frac{5 p_{\text{e}}}{2 m_{\text{e}} \nu_{\text{ee}}}, \quad \nu_{\parallel} = \frac{p_{\text{i}}}{\rho \nu_{\text{ii}}}, \quad (9)$$

where  $p_i$  ( $p_e$ ) is the ion (electron) pressure,  $\nu_{ii}$  ( $\nu_{ee}$ ) is the ion-ion (electron-electron) Coulomb collision frequency and  $m_e$  is the electron mass.

The Knudsen number,  $\text{Kn}$ , is a useful measure of the collisionality of the plasma with the collisionless (collisional) limit corresponding to  $\text{Kn}^{-1} \ll 1$  ( $\text{Kn}^{-1} \gg 1$ ). It is defined as

$$\text{Kn} \equiv \frac{\lambda_i}{H}, \quad (10)$$

where  $\lambda_i = c/\nu_{ii}$  is the ion mean free path,  $c = \sqrt{p/\rho}$  is the isothermal sound speed, and  $H = c^2/g$  is the pressure scale height of the plasma. In terms of the Knudsen number, the heat diffusivity,  $\kappa_{\parallel} = \chi_{\parallel} T/p$ , and the Braginskii viscosity coefficient,  $\nu_{\parallel}$ , are given by (Kunz et al. 2012)

$$\kappa_{\parallel} \approx 24 \text{Kn} cH, \quad \nu_{\parallel} \approx 0.48 \text{Kn} cH. \quad (11)$$

Note here that the collisionless limit,  $\text{Kn}^{-1} \ll 1$ , corresponds to high values of  $\kappa_{\parallel}$  and  $\nu_{\parallel}$ , i.e., fast transport. Finally, it is useful to define the plasma- $\beta$  as  $\beta = 2c^2/v_a^2$  where the Alfvén speed is given by  $v_a = B/\sqrt{4\pi\rho}$ . In the outskirts of galaxy clusters, estimated values for the dimensionless numbers are  $\beta \sim 10^2$ – $10^4$  and  $\text{Kn}^{-1} \sim 10$ – $100$  (Carilli & Taylor 2002; Vikhlinin et al. 2006).

### 2.3 The ‘standard’ subgrid model for viscosity

Equation (8) shows that a pressure anisotropy naturally arises in a weakly collisional plasma because of changes in magnetic field strength or plasma density. The mirror and firehose instabilities become active if the magnitude of the pressure anisotropy is comparable to the magnetic energy density. This is more likely to occur if the magnetic field strength is weak, as it is in the ICM. These microscale instabilities are not correctly described by the equations of Braginskii MHD. PIC simulations (e.g. Kunz et al. 2014) and solar wind observations (e.g. Bale et al. 2009; Chen et al. 2016) indicate that the microscale instabilities grow extremely quickly and act to remove excess pressure anisotropy to sustain marginal stability on average. Motivated by these studies, a common subgrid model for  $\Delta p$  consists of limiting its value to lie within the thresholds for stability of the firehose and mirror instability (e.g. Sharma et al. 2006; Kunz et al. 2012; Squire et al. 2017a). We employ this subgrid model and limit  $\Delta p$  by

$$-\frac{B^2}{4\pi} < \Delta p < \frac{B^2}{8\pi}, \quad (12)$$

when evaluating the viscosity tensor in our simulations.

### 2.4 The subgrid model for suppressed heat conduction

Komarov et al. (2016) found that the heat conductivity in a mirror-unstable plasma is reduced by a suppression factor  $S_D \approx 0.2$  compared to the Spitzer value. This result was found by extracting magnetic field lines from the hybrid-kinetic (kinetic ions, fluid electrons) PIC simulation presented in Kunz et al. (2014) and studying the effect of magnetic mirrors on the electron dynamics. The suppression of heat conductivity arises due to a combination of electron trapping in magnetic mirrors (which prevents them from contributing to conduction) and a decrease in the effective mean-free-path of collisions for the untrapped electrons.

Motivated by these results, we replace  $\chi_{\parallel}$  with an effective heat conductivity

$$\chi_{\text{eff}} = S_D \chi_{\parallel} \quad (13)$$

in the regions where the ions are unstable according to the linear stability criterion for the mirror instability. This subgrid model for the heat conductivity is designed to mimic the behaviour seen in more realistic (but small-scale) models in the simplest manner. The mirror instability becomes unstable when

$$\Delta p \gtrsim \frac{B^2}{8\pi}, \quad (14)$$

and by combining equation (8) and equation (11) we can rewrite this condition for the mirror instability (and the consequent suppression of heat conductivity) can be rewritten as

$$0.48(3bb : \nabla \mathbf{v} - \nabla \cdot \mathbf{v}) \frac{H}{c} \gtrsim \frac{\text{Kn}^{-1}}{\beta}. \quad (15)$$

Equation (15) predicts that plasmas are more prone to the mirror instability when  $\beta \text{Kn} \gg 1$ , i.e., when the magnetic field is weak and collisions are rare. The subgrid model for suppression of heat conductivity is thus predicted to become active in this limit. We find it is useful to understand how plasma dynamics are modified in the two extreme regimes,  $S_D = 0.01$  (almost full suppression) and  $S_D = 1$  (no suppression), and consequently perform most of our simulations with these parameters. We do however return to the value motivated by Komarov et al. (2016),  $S_D = 0.2$ , in Section 4.

## 3 THE MAGNETO-THERMAL INSTABILITY

### 3.1 Numerical setup

We consider the numerical setup described in Kunz et al. (2012), i.e. an MTI unstable region with anisotropic heat conductivity and Braginskii viscosity sandwiched between two stable regions with isotropic heat conductivity (see also Parrish & Stone 2007). For completeness, the profiles for the temperature<sup>1</sup>,  $T(z)$ , and density,  $\rho(z)$ , are given by (Parrish & Stone 2005; McCourt et al. 2011; Kunz et al. 2012)

$$\rho(z) = \rho_0 \left(1 - \frac{z}{3H}\right)^2, \quad (16)$$

$$T(z) = T_0 \left(1 - \frac{z}{3H}\right), \quad (17)$$

where  $z$  is the vertical coordinate and  $H$  is the scale height at the lower boundary of the unstable domain. These profiles satisfy hydrostatic equilibrium

$$\frac{\partial p}{\partial z} = -\rho g, \quad (18)$$

in a (constant) gravitational field with  $g = k_B T_0 / (H \mu m_H)$ . Here the pressure is given by the equation of state in which we assume that the composition of the plasma is constant.<sup>2</sup> The temperature decreases in the direction opposite to the direction of gravity. We include an initially horizontal magnetic field which makes the atmosphere maximally unstable to the MTI. The magnetic field strength is spatially constant and is characterized by the plasma- $\beta$  at the bottom of the unstable domain,  $\beta_0$ . In our simulation analysis, the

<sup>1</sup> We assume that the ions and electrons have the same temperature. The low collisionality however leads to a long temperature equilibration time scale in the outskirts of clusters.

<sup>2</sup> See Pessah & Chakraborty (2013), Berlok & Pessah (2015), Berlok & Pessah (2016a), and Berlok & Pessah (2016b) for studies that relax this assumption.

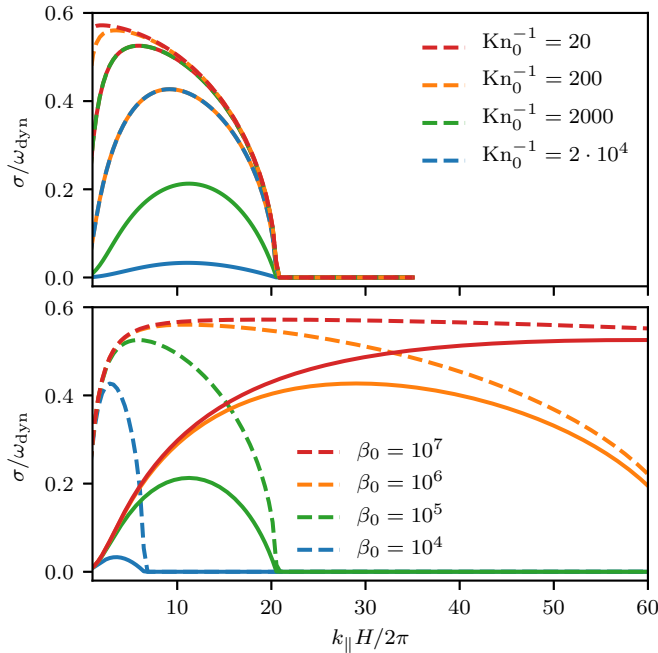


**Figure 1.** Growth rates as function of mode number,  $n = k_{\parallel} H/2\pi$ , calculated at the bottom of the unstable domain, for a variety of collisionalities for  $\beta_0 = 10^5$  (upper panel) and for a variety of  $\beta_0$ 's for  $\text{Kn}_0^{-1} = 2000$  (lower panel). Solid lines show theoretical growth rate for a heat conductivity which is smaller by a factor  $S_D = 0.01$  with respect to the corresponding dashed line.

energy densities are given in units of  $\rho_0 c_0^2$  where  $\rho_0$  ( $c_0$ ) is the density (isothermal sound speed) at the bottom of the unstable domain. Similarly, the inverse Knudsen number at this location is designated  $\text{Kn}_0^{-1}$ . The boundary conditions at the top and bottom of the computational domain maintain hydrostatic equilibrium by extrapolating density and pressure while keeping the temperature fixed. In addition, the velocity is reflected and the magnetic field is forced to remain horizontal. Our boundary conditions are described in further detail in Appendix B1 in [Berlok & Pessah \(2016a\)](#).

We use the publicly available MHD code Athena ([Stone et al. 2008](#); [Stone & Gardiner 2009](#)) to evolve equations (2)–(5) in time. The implementation of anisotropic heat conduction is described in [Parrish & Stone \(2005\)](#); [Sharma & Hammett \(2007\)](#) and anisotropic viscosity in [Parrish et al. \(2012b\)](#). The time step constraint on explicit solution of these parabolic diffusion equations makes the simulations very computationally demanding. We use sub-cycling with 10 diffusion steps per MHD step as in [Kunz et al. \(2012\)](#) but note that future studies could likely benefit from using super timestepping methods ([Meyer et al. 2012](#); [Vaidya et al. 2017](#); [Berlok et al. 2019](#)). We present two-dimensional (2D) simulations in Sections 3.3–3.5 and three-dimensional (3D) simulations in Section 3.6. Tables C1 and C2 in Appendix C give an overview of the parameters and numerical resolutions used in the simulations.

### 3.2 Expectations from local, linear theory

The MTI arises as a consequence of heat conduction along magnetic field lines in a thermally stratified atmosphere ([Balbus 2000, 2001](#)). The growth rate of the MTI is therefore intimately connected to the magnitude of the heat conductivity,  $\chi_{\parallel}$ . Here we use the local, linear theory of [Kunz \(2011\)](#) to estimate the change in growth rate when the heat conductivity is suppressed by a factor  $S_D = 0.01$ .

[Kunz \(2011\)](#) included the effect of Braginskii viscosity in the derivation of a local, linear dispersion relation for the MTI. It was found that the maximum growth rate occurs for wave vectors parallel to the magnetic field,  $k = k_x$ , and that this mode of instability is unaffected by Braginskii viscosity. We therefore calculate the MTI growth rate as a function of  $k = k_x$  for various values of  $\text{Kn}_0^{-1}$  (which sets the heat conductivity, see equation 11) and  $\beta_0$ . The results are shown in Fig. 1 where  $\text{Kn}_0^{-1}$  is varied in the upper panel at fixed  $\beta_0 = 10^5$  and  $\beta_0$  is varied in the lower panel at fixed  $\text{Kn}_0^{-1} = 2000$ . Here the growth rate,  $\sigma$ , is measured with respect to the dynamical frequency,  $\omega_{\text{dyn}} = c_0/H$ , at the bottom of the unstable domain. The upper panel of Fig. 1 shows that increasing  $\text{Kn}_0^{-1}$  decreases the growth rate at all wavelengths. At the same time, the fastest growing mode is shifted to shorter wavelengths. As previously explained, this was expected as the MTI depends on efficient heat conduction and higher  $\text{Kn}_0^{-1}$  translates to lower  $\chi_{\parallel}$ . Each dashed line has a corresponding solid line (with the same color) where the heat conductivity has been suppressed by a factor  $S_D = 0.01$ . Interestingly, the reduction in MTI growth rate depends on how fast the heat conduction is without suppression. For instance, the maximal growth rate for  $\text{Kn}_0^{-1} = 2 \times 10^4$  (blue dashed curve) is  $\sigma_{\text{max}}/\omega_{\text{dyn}} = 0.43$  while it is only  $\sigma_{\text{max}}/\omega_{\text{dyn}} = 0.03$  when suppressed (blue solid curve). With faster heat conduction, e.g.  $\text{Kn}_0^{-1} = 20$ , the fastest growth rate is only slightly reduced (from  $\sigma_{\text{max}}/\omega_{\text{dyn}} = 0.57$  to  $\sigma_{\text{max}}/\omega_{\text{dyn}} = 0.53$ ). In conclusion, suppression of heat conduction completely quenches the MTI if the heat conductivity is already low but if the unsuppressed heat conductivity is high, the suppression of heat conduction only leads to a moderate reduction in the growth rate.

In the lower panel of Fig. 1 we show the dependence of the growth rates on  $\beta_0$ . The trend is that the growth rates increase with  $\beta_0$  and that the fastest growing mode shifts to shorter wavelengths. The explanation for this behavior is that magnetic tension inhibits or even quenches the instability when  $\omega_a \gg \omega_{\text{dyn}}$  where  $\omega_a = k_{\parallel} v_a$  is the Alfvén frequency. This means that growth of the MTI is prevented when  $k_{\parallel} H \gg \sqrt{\beta_0/2}$ . Each dashed line again has a corresponding solid line where the heat conductivity is suppressed with  $S_D = 0.01$ . At low  $\beta_0$  ( $10^4$  and  $10^5$ ), the suppression of heat conductivity leads to a severe reduction in the MTI growth rate. At high  $\beta_0$  ( $10^6$  and  $10^7$ ), the reduction in the maximal growth rate is however only moderate.

The results in Fig. 1 can be explained in terms of the ratio of conduction frequency to the dynamical frequency. Here the conduction frequency

$$\omega_c = \frac{2}{5} \kappa_{\parallel} k_{\parallel}^2, \quad (19)$$

sets the inverse time scale for heat conduction across a mode with parallel wavelength,  $k_{\parallel}$ . Significant growth of a given MTI mode depends on whether it is in the fast conduction limit,  $\omega_c/\omega_{\text{dyn}} > 1$  or not. Whether a mode is quenched by suppression of heat conductivity (or whether the growth rate is only moderately modified) then depends on whether the mode retains  $\omega_c/\omega_{\text{dyn}} > 1$  or whether  $\omega_c/\omega_{\text{dyn}} < 1$  after suppression.

As a function of the mode number,  $n = k_{\parallel} H/2\pi$  and using equation (11) the ratio  $\omega_c/\omega_{\text{dyn}}$  can be estimated as

$$\frac{\omega_c}{\omega_{\text{dyn}}} \approx S_D \frac{380}{\text{Kn}_0^{-1}} n^2, \quad (20)$$

At high  $\beta_0$ ,  $\omega_c/\omega_{\text{dyn}}$  remains large because the fastest growing mode has very high  $n$  (due to weak magnetic tension). Physically,



the time scale for heat transport across the mode is short even with suppression because the spatial scales are small.

More quantitatively, magnetic tension prevents growth when  $k_{\parallel} H \gg \sqrt{\beta_0/2}$ , such that the mode number that gives the maximum growth rate,  $n_{\max}$ , will scale as  $\sqrt{\beta_0}$ . This leads to the scaling  $\omega_c/\omega_{\text{dyn}} \propto S_D \beta_0 / \text{Kn}_0^{-1}$ . The linear theory thus indicates that the fastest growing MTI mode can remain in the fast heat conduction limit if  $\beta_0 / \text{Kn}_0^{-1} \gg 1$  is large. Incidentally,  $\beta_0 / \text{Kn}_0^{-1} \gg 1$  large is precisely the limit where the mirror instability is likely to take place and lead to suppression of heat conductivity (see equation 15). In the opposite limit,  $\beta_0 / \text{Kn}_0^{-1}$  small, the MTI growth rate can be severely reduced by a suppression of heat conductivity. In this limit, however, such suppression is unlikely to take place because the mirror instability is not as easily excited (see also equation 15).

In conclusion, both the MTI and the mirror instability take their most vigorous form in a plasma in which the magnetic field is weak (large  $\beta_0$ ) and the collisionality is low (small  $\text{Kn}_0^{-1}$ ). In this regime, the MTI grows fast because *i*) the heat conductivity,  $\chi_{\parallel}$ , is high and *ii*) a weak magnetic field only prevents growth on small scales (across which heat conduction remains fast). In this regime, the MTI growth rates remain dynamically important even if the heat conductivity is suppressed by a significant factor, e.g.,  $S_D = 0.01$ . This observation will become important for interpreting our nonlinear simulations in Section 3.5.

### 3.3 Interruption of an eigenmode of the MTI

We illustrate how the linear stage of the MTI can be interrupted if the heat conductivity is reduced in mirror-unstable regions. This test of our numerical setup is performed by initializing a simulation with an MTI eigenmode. While the MTI mechanism is intrinsically local and therefore well described by local, linear theory (Kunz 2011 and Section 3.2), the  $z$ -dependence of background variables in our setup (i.e. temperature as well as density and pressure gradients, see equations 16–18) make the fastest growth rate obtained using local, linear theory differ by around 20 % between the top and bottom of the unstable domain. Consequently, seeding with a local eigenmode does not give an exact match between theory and simulation. In order to obtain a completely clean evolution of an eigenmode, we therefore derive the linearized equations without making the local approximation in  $z$ . The resulting eigenvalue problem is solved for the eigenmodes and corresponding growth rates using PSECAS (Berlok & Pfrommer 2019). The linearized equations and details on this procedure, which share features with the quasi-global theory for a vertical magnetic field (Latter & Kunz 2012; Berlok & Pessah 2016b), are outlined in Appendix B. For consistency with the boundary conditions used in the linear theory, the eigenmode-seeded simulation is performed with reflective boundary conditions and without the stable buffer regions that we use in the simulations of the nonlinear regime. We note that these boundary conditions cause the eigenmodes to have a larger pressure anisotropy than found for the fastest growing mode using local linear theory (see details in Appendix B).

We show the time evolution of an exactly seeded simulation where the background<sup>3</sup> has  $\beta_0 = 10^6$  and  $\text{Kn}_0^{-1} = 2000$  in Fig. 2.

<sup>3</sup> This combination of  $\beta_0$  and  $\text{Kn}_0^{-1}$  is chosen such that modification of the MTI evolution occurs already early in the linear stage of the instability. This gives a time interval of  $\approx 5t_0$  during which the perturbation amplitude (and corresponding non-linearities) are small enough that the modifications seen are due to the suppressed heat conductivity.

Here the eigenmode used for seeding the instability has  $k_x H / 2\pi = 1$  and growth rate  $\sigma t_0 = 0.28305$  where  $t_0 = \omega_{\text{dyn}}^{-1} = H / c_0$  (for comparison, the fastest growing mode has  $\sigma t_0 = 0.64700$  and occurs at  $k_x H / 2\pi = 13.8374$ . See Fig. B2 in Appendix B). The first row of panels in Fig. 2 shows the magnetic field lines (black solid lines) and temperature evolution (red is hot, blue is cold). The atmosphere is vertically stratified with temperature that decreases with height and gravity acts downwards. The system is unstable to the MTI and the magnetic field lines start to bend due to buoyant motions that grow exponentially in time.<sup>4</sup> The motions driven by MTI have an associated pressure anisotropy which can excite microscale instabilities. The second row of panels shows  $4\pi\Delta p/B^2$  which is a measure of whether the pressure anisotropy,  $\Delta p$ , exceeds the mirror threshold ( $4\pi\Delta p/B^2 > 1/2$ ) or the firehose threshold ( $4\pi\Delta p/B^2 < -1$ ). Mirror-unstable (firehose-unstable) regions appear as saturated orange (purple) patches in the last three panels. The heat conductivity,  $\chi_{\parallel}$ , is reduced by a factor  $S_D = 0.01$  in the mirror-unstable regions. Maps of  $\chi_{\parallel}$ , in which regions with suppressed thermal conductivity appear as purple patches, are shown in the third row of panels in Fig. 2. Note here that values for  $\chi_{\parallel}$  are shown normalized by  $\chi_0$ , the initial value at the bottom of the unstable domain. The regions with suppressed heat conductivity are predicted by the quasi-global theory to initially appear at the top center and bottom left- and right hand sides of the computational domain. This appearance is indeed seen in the heat conductivity map at  $t = 6t_0$ . The additional high-frequency striations are not predicted by the linear theory. These features are spatially correlated with variations in  $\nabla \cdot \mathbf{v}$ , as evident by comparing the third and fourth rows of Fig. 2. This indicates that the small scale variations in heat conductivity are related to compressible motions of the plasma. These features occur on the grid scale which make them problematic from a numerical point of view. We therefore dedicate two appendices (A and C) in order to ensure that our main conclusions are unaffected by the striations. We briefly summarize why we believe the striations occur below.

Sound waves are compressible and can drive a pressure anisotropy by modifying the density. This means that high amplitude sound waves can trigger the mirror instability, such that sound waves, in combination with our subgrid model for heat conduction (Section 2.4), can lead to a reduction in heat conductivity. A study of this phenomenon, including a theoretical amplitude limit on sound waves (equation A7), is described in Appendix A. This study shows that sound wave evolution can be modified and give rise to a jagged appearance in pressure anisotropy and heat conductivity which looks remarkably similar to the features seen in the MTI simulation. Given the visual resemblance and the spatial correlation with the velocity divergence, we therefore suspect that the striations seen in Fig. 2 are due to sound waves triggering the mirror instability.

While excitation of the mirror instability by low-amplitude sound waves in this context is an unwanted consequence of the subgrid model for heat conduction (due to the resulting grid scale features), Kunz et al. (2020) have very recently showed that high-amplitude sound waves can excite the mirror instability in collisionless systems. Using kinetic analysis and PIC simulations, they found that the (ion) heat conductivity is suppressed in the mirror unstable regions. Further details and discussion about triggering of the mirror instability by sound waves can be found in Appendix A.

<sup>4</sup> This simulation stops early, and the magnetic field bending is only barely visible at  $t = 12t_0$ . A nonlinear simulation will be shown in Section 3.4.

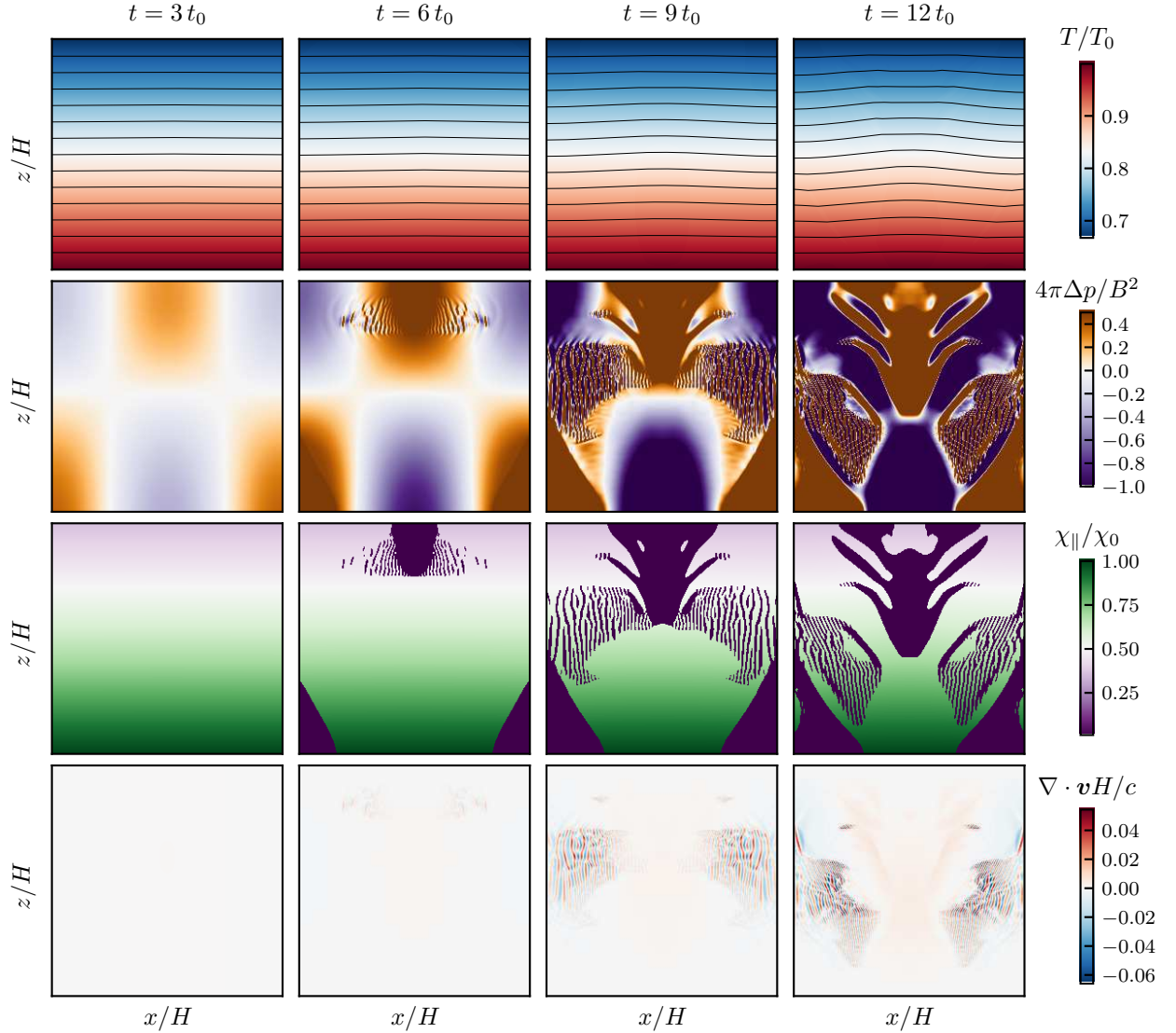


**Figure 2.** Interruption of the MTI in an ATHENA simulation seeded with an eigenmode obtained with PSECAS. First row: Temperature evolution with magnetic field lines (initially horizontal) indicated with solid black lines. Second row: Pressure anisotropy attains large positive values and a large fraction of the domain becomes mirror unstable and become suppressed by our subgrid model for heat conduction, see Sect. 2.4. Third row: The heat conductivity,  $\chi_{||}$ . At later times, mirror-unstable regions appear as purple patches in which the heat conductivity is suppressed. Fourth row: Divergence of the velocity field, which is spatially correlated with striations in the heat conductivity. The spatial extent shown has size  $H \times H$  where  $H$  is the scale height.

In particular, we discuss how simulations converge despite the grid scale striations in heat conductivity found in regions with  $\nabla \cdot \mathbf{v} \neq 0$ .

We now proceed with the analysis of the simulation shown in Fig. 2 by taking cuts at constant height. Fig. 3 shows cuts at  $z/H = 1/5$  and compares results from the simulation (solid lines) with the linear theory (dashed lines). The linear theory does not take into account the subgrid models (nor non-linear terms in the governing equations) and the eigenmode thus retains its original shape while its amplitude grows exponentially as time progresses from the left-hand side to the right-hand side in Fig. 3. We fit the exponential growth in the perturbed variables and find essentially perfect agreement with the PSECAS solution until the onset of suppressed conductivity (see Fig B3 in Appendix B). In the first panel ( $t/t_0 = 3$ ) in Fig. 3, the pressure anisotropy is below the mirror threshold, and the simulation agrees with the linear theory. At later times, the profiles in the simulation start to deviate from the sinusoidal shapes of the linear theory. This is because the pressure anisotropy limiters and associated suppression of heat conductivity have begun to mod-

ify the evolution. The deviation is particularly evident at  $t/t_0 = 6$  and 9 where the temperature has acquired doubly-peaked profiles and  $\Delta p$  is limited by equation (12). Here the mirror-infested regions, in which the heat conductivity is suppressed, are indicated with orange solid lines. In the last panel ( $t/t_0 = 12$ ), both the velocity and temperature profile have acquired highly complex shapes with small regions that spatially fluctuate between being mirror-infested and retaining full Spitzer conductivity. Suppression of the thermal conductivity in mirror-unstable regions thus disrupts the otherwise clean evolution of an MTI eigenmode.

### 3.4 Nonlinear simulations

We proceed by performing nonlinear simulations which are seeded with Gaussian, subsonic velocity perturbations with amplitude

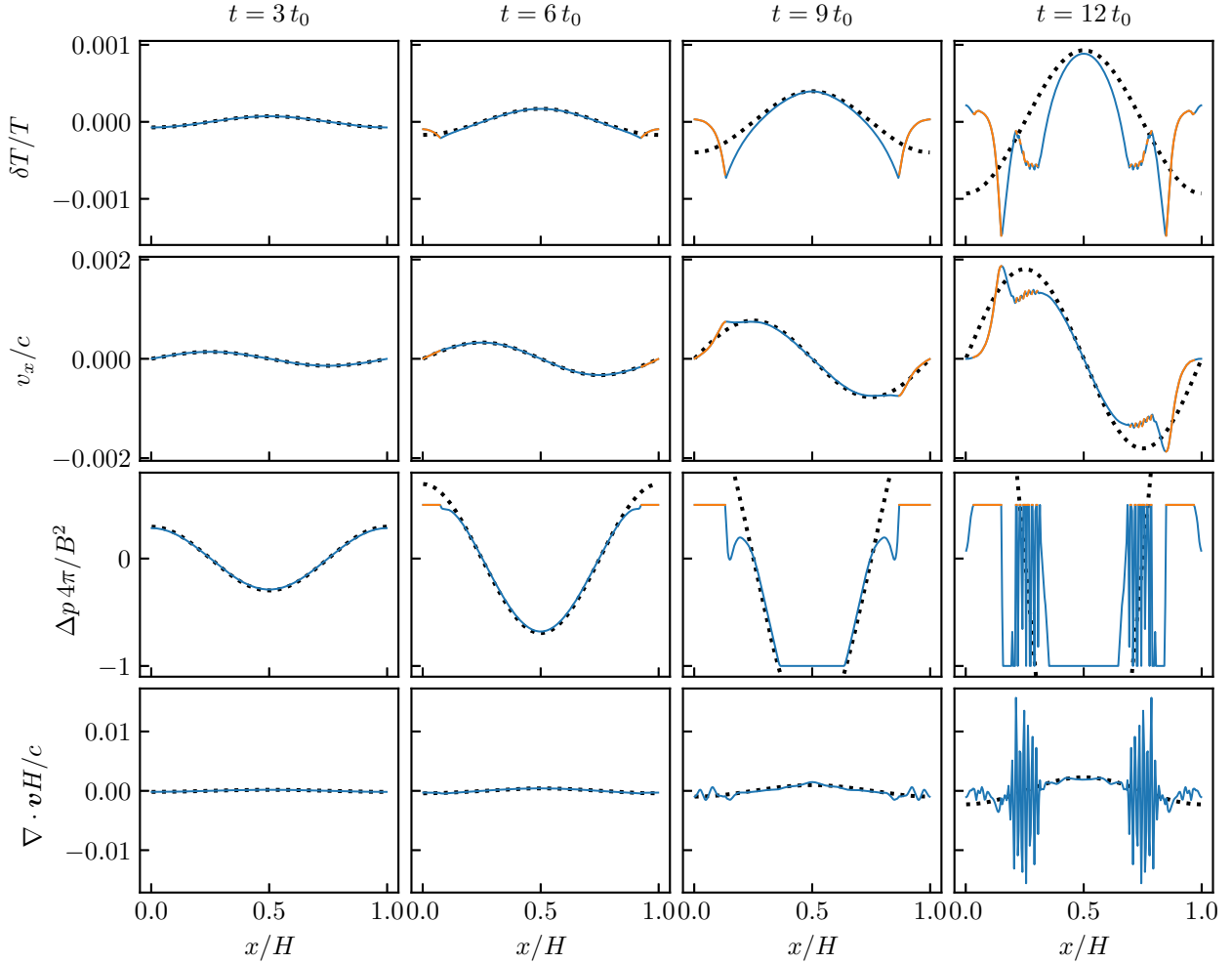


**Figure 3.** Horizontal profiles at  $z/L = 1/5$  from the simulation shown in Fig. 2. The rows show  $\delta T/T$  (first row),  $v_x/c$  (second row),  $4\pi\Delta p/B^2$  (third row), and  $\nabla \cdot \mathbf{v}H/c$  (fourth row). The evolution of the ATHENA simulation (solid lines) is well described by the PSECAS eigenmode solution (dotted lines) until the mirror instability threshold is surpassed. Subsequently, mirror-unstable regions and resulting suppression of heat conductivity leads to an interruption of the eigenmode.

$10^{-4}c$ .<sup>5</sup> We compare simulations with and without heat transport suppression in order to understand whether the subgrid model for heat transport modifies the saturated state of the MTI. The simulations have initial magnetic field strength with  $\beta_0 = 10^5$  and the inverse Knudsen number is  $\text{Kn}_0^{-1} = 2000$ .<sup>6</sup> The simulations with and without suppression have  $S_D = 0.01$  and  $S_D = 1$ , respectively. Note that this is in the regime of  $\beta_0$  and  $\text{Kn}_0^{-1}$  where  $S_D = 0.01$  does not significantly change the linear growth rate of the MTI, see Fig. 1.

The evolution of the MTI in the simulation with  $S_D = 0.01$  is presented in Fig. 4. The initially horizontal magnetic field with a temperature gradient pointing downwards leads to the generation of buoyant motions which change the magnetic field strength and structure (first row of panels). The inclusion of Braginskii viscosity

suppresses small scale motions and the dominant modes of the MTI grow on larger scales than in a simulation with only anisotropic heat conduction (Kunz et al. 2012). This is the case even though the limiters, equation (12), make the simulation less viscous than a simulation without them (the difference in magnetic field line morphology between simulations with unlimited Braginskii viscosity, limited Braginskii viscosity, and zero viscosity is clearly illustrated in figure 17 in Kunz et al. 2012, see also figure 5 in Berlok & Pessah 2016b).

The plasma motions created by the MTI in turn lead to the generation of a non-zero pressure anisotropy, as given by equation (8). We show the spatial evolution of the pressure anisotropy in the middle row and the corresponding heat conductivity in the bottom row of Fig. 4. At  $t/t_0 = 10$ , the pressure anisotropy is still below the mirror instability threshold and the heat conductivity takes the full Spitzer value. At  $t/t_0 = 15$ , the mirror threshold has been exceeded and purple large-scale regions of suppressed heat conductivity appear. At  $t/t_0 = 25$ , the purple patches have progressed to smaller scales with striations similar to the ones found in Fig. 2. We again find that these features are spatially correlated with the velocity divergence (not shown).

At  $t/t_0 = 25$ , roughly fifty percent of the computational domain

<sup>5</sup> While we initialize the simulations as a quiescent cluster, we note that real cluster outskirts are expected to be turbulent due to mergers and gas accretion. This limitation of our idealized setup is discussed in Sections 3.6 and 4.

<sup>6</sup> The heat diffusivity and the Braginskii viscosity coefficient are then given by  $\kappa_{\parallel} = \chi_{\parallel} T/p = 0.012 T^{5/2}/\rho$  and  $\nu_{\parallel} = 2.4 \times 10^{-4} T^{5/2}/\rho$  in code units, see Kunz et al. (2012) for details.

is unstable to the mirror instability according to the linear stability criterion. Near the end of the simulation (fourth and fifth panels of Fig. 4, at  $t/t_0 = 40$  and  $50$ ), however, less than 10 per cent of the computational domain is unstable according to the linear stability criterion for the mirror instability. The low fraction of the mirror unstable volume is probably related to the growth in magnetic field strength. While magnetic field growth is necessary in order to generate positive pressure anisotropies (which will lead to triggering of the mirror instability) an increased magnetic field strength also decreases the plasma- $\beta$ . This can have the side-effect that the increased magnetic field strength ends up stabilizing the mirror instability. That is,  $B^2/8\pi < \Delta p \propto dB/dt$  becomes more difficult to achieve as  $B$  grows in magnitude and  $dB/dt$  saturates.

In a simulation seeded with Gaussian velocity components, the evolution of the MTI is such that the plasma almost entirely avoids becoming unstable to the firehose instability by arranging magnetic field lines to lie across velocity gradients, see [Kunz et al. \(2012\)](#). We have checked this by using the instability criterion for the firehose, see equation (12) and the maps of  $4\pi\Delta p/B^2$  in the middle row of Fig. 4. Note that this differs from a simulation seeded with an MTI eigenmode where a significant region of space becomes firehose unstable (see Fig. 2). We analyze the simulations quantitatively by considering the time evolution of a number of key quantities.

The upper, left-hand panel of Fig. 5 shows the vertical kinetic and magnetic energies,  $\langle \rho v_z^2/2 \rangle$  and  $\langle B_z^2/8\pi \rangle$ , where  $\langle \rangle$  denotes an average over the unstable part of the computational domain ( $0.5 < z/H < 1.5$ ). The simulation with  $S_D = 0.01$  starts to deviate from the reference simulation with  $S_D = 1$  at around  $t/t_0 = 15$ . This deviation occurs because a substantial fraction of the volume is mirror-unstable, so that the effective heat conductivity is suppressed, inhibiting the growth. The deviation between the simulation with  $S_D = 0.01$  and the one with  $S_D = 1$  is however only temporary. In the end, the energies in the saturated states are roughly similar.

In order to further quantify this surprising result, we define  $\xi$  to be the ratio of the vertical magnetic energy in  $S_D = 0.01$  and  $S_D = 1$  simulations, i.e.,

$$\xi \equiv \frac{\langle B_z^2(S_D = 0.01) \rangle}{\langle B_z^2(S_D = 1) \rangle}. \quad (21)$$

The advantage gained by considering  $\xi$  instead of the energies is that  $\xi$  does not vary by many orders of magnitude. We show the evolution of  $\xi$  in the upper right-hand panel of Fig. 5. While the value dips down to less than 10 per cent at around  $t/t_0 = 25$  it saturates with a value close to unity in the end.

We also consider the fraction of the computational domain that is unstable to the mirror instability (lower, left-hand panel of Fig. 5). Due to the subgrid model employed, this is a measure of the reduction of the heat conductivity. We observe that the start and end of the dip in  $\xi$  are roughly coincident in time with the peak in and subsequent decay of the mirror unstable fraction.

Finally we consider the volume average of the absolute value of the field-aligned temperature gradient, i.e.

$$\phi_T = \left\langle \left| \mathbf{b} \cdot \nabla T \right| \frac{H}{T} \right\rangle. \quad (22)$$

At first sight,  $\phi_T$  might appear to be a purely geometrical construct but as we will argue here,  $\phi_T$  is a measure of the efficiency of heat transport along magnetic field lines. The minimum value of  $\phi_T$  is zero and occurs in the limit of infinitely fast heat conduction where closed magnetic field lines become isotherms. In the opposite limit, where heat conduction is absent, the expected upper bound on the value of  $\phi_T$  is the one found with a magnetic field everywhere

perfectly aligned with the initial temperature gradient ( $\mathbf{b} = \mathbf{e}_z$ ). Using equation (17), we find this value to be  $\phi_T = 1/3$ . Hence, we expect  $\phi_T$  to be large in simulations where the heat conductivity is low (either due to a large  $\text{Kn}_0^{-1}$  or to a high percentage of the domain being unstable to the mirror instability) and small in simulations where the heat conductivity is fast.

We show the time evolution of  $\phi_T$  in the lower, right-hand panel of Fig. 5, again comparing with the reference simulation. Due to the suppression of  $\chi_{\parallel}$ , the simulation with  $S_D = 0.01$  attains a somewhat higher value of  $\phi_T$  than the reference simulation with  $S_D = 1$ . However, this only occurs during the period of time where a significant volume fraction is mirror-unstable (compare the lower left-hand panel of Fig. 5 with the lower right-hand panel).

### 3.5 Parameter study

In the previous section we found that the MTI is quite robust to suppression of heat conductivity, at least when  $\beta_0 = 10^5$  and  $\text{Kn}_0^{-1} = 2000$ . Here we perform a parameter study in order to see whether there are other parameter regimes where the MTI is more severely modified. We vary the collisionality, via  $\text{Kn}_0^{-1}$  at fixed  $\beta_0 = 10^5$  (left-hand column of Fig. 6) and the magnetic field strength, via  $\beta_0$ , at fixed  $\text{Kn}_0^{-1} = 2000$  (right-hand column of Fig. 6). We show in Fig. 6 the evolution of vertical magnetic energy (first row), the ratio of magnetic energy in simulations with and without suppression,  $\xi$ , (second row, see equation 21), the mirror-unstable fraction (third row) and the field-aligned temperature gradient,  $\phi_T$  (fourth row, see equation 22). The solid lines correspond to simulations with heat transport suppression ( $S_D = 0.01$ ) and the dashed lines are references with full Spitzer conductivity ( $S_D = 1$ ).

The left- and right-hand panels of Fig. 6 have many features in common. This is because the important parameter for mirror instability (see equation 15),  $\beta_0 \text{Kn}_0$ , only takes four different values, i.e.,  $\beta_0 \text{Kn}_0 = 5, 50, 500$  and  $5000$ . For  $\beta_0 \text{Kn}_0 = 5$  (shown with blue lines in Fig. 6), the simulation with suppression is virtually indistinguishable from the reference simulation. The explanation is simply that the mirror-instability threshold is almost never surpassed in these simulations (third row in Fig. 6). For  $\beta_0 \text{Kn}_0 = 50$  (shown with orange lines in Fig. 6), a very significant volume fraction ( $> 60\%$ ) is mirror-unstable at  $t/t_0 \approx 20$  but the fraction goes down to 10% at the end of the simulation. This is evidently not enough to effectively suppress heat transport (i.e., the deviation in  $\phi_T$  is temporary) and the saturated energies in the  $S_D = 0.01$  simulation are similar to the reference simulation. When  $\beta_0 \text{Kn}_0 = 500$  (green lines), the final mirror-unstable fraction is  $\approx 20\%$  and the saturated energies still do not differ by much between the  $S_D = 0.01$  and  $S_D = 1$  simulations. The  $\xi$  parameter in fact indicates that there is  $\approx 25\%$  more energy in the  $S_D = 0.01$  simulation with  $\text{Kn}_0^{-1} = 200$ . This is however within the uncertainty given by a finite numerical resolution (see Appendix C for a convergence study and Tables C1 and C2 for an overview of the numerical resolutions used in our simulations). Finally, for an extreme value of  $\beta_0 \text{Kn}_0 = 5000$ , the mirror-unstable fraction remains above 40 % at the end of the simulation, and the simulations with  $S_D = 0.01$  saturate with slightly less energy than the reference simulation ( $\xi \approx 3/4$  at the end).

The trends outlined above can be understood using the MTI linear theory (see Section 3.2). Here we found that systems with large  $\beta_0$  and small  $\text{Kn}_0^{-1}$  (i.e. large  $\beta_0 \text{Kn}_0$ ) to be the most susceptible to the mirror instability and to have the largest MTI growth rates (when calculated using the full Spitzer conductivity). In this regime, the fastest mode of the MTI is so deeply in the fast heat conduction limit that suppression of the heat conductivity only slightly lowers



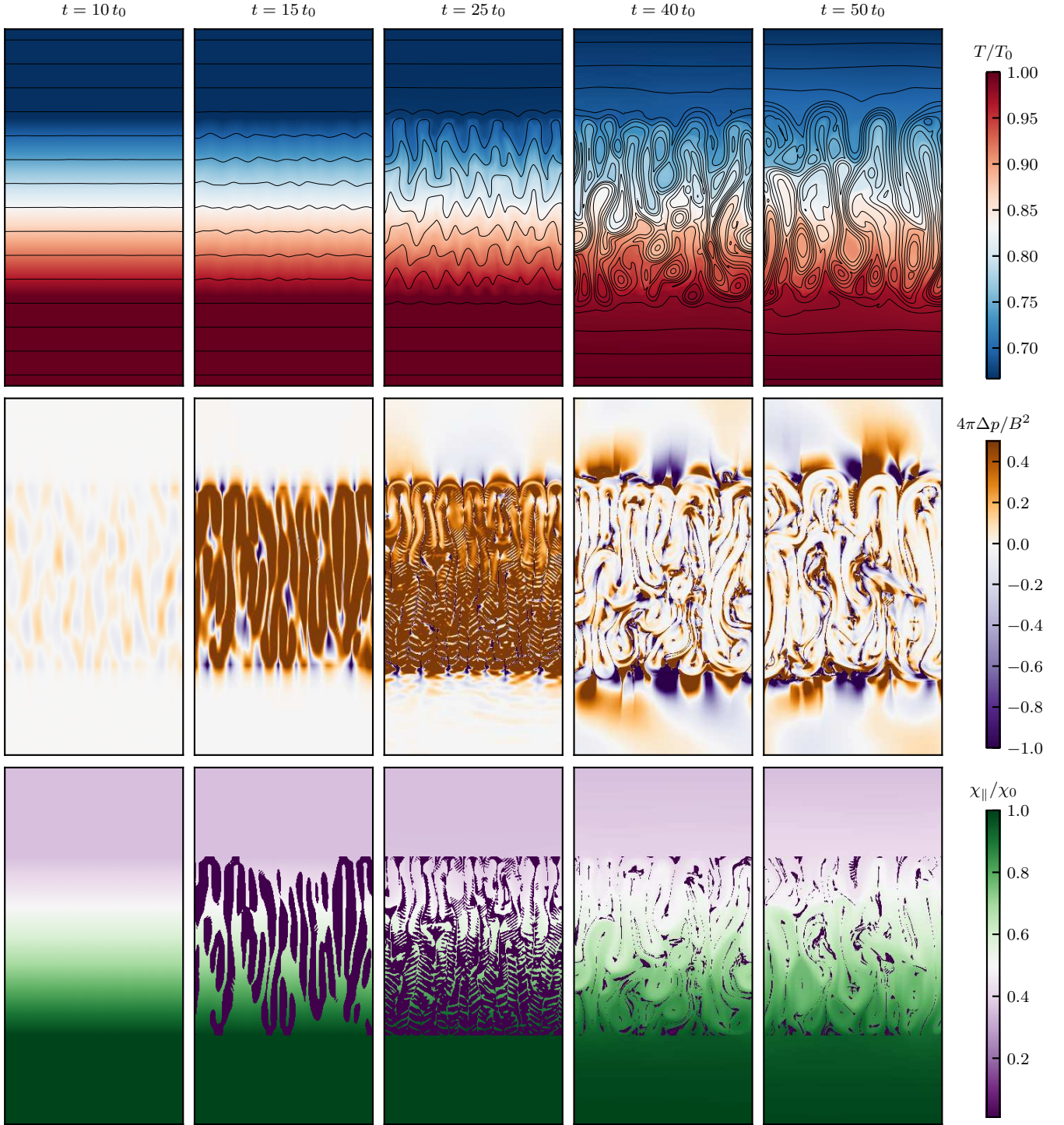


**Figure 4.** Evolution of temperature and magnetic field (upper row), pressure anisotropy (middle row), and heat conductivity (bottom row) in a simulation with  $\text{Kn}_0^{-1} = 2000$ ,  $\beta_0 = 10^5$  and  $S_D = 0.01$ . The computational domain has size  $H \times 2H$  but only the middle half of the domain is unstable to the MTI. The top and bottom regions are stable, isothermal buffers which shield the central region from the reflective boundaries.

the growth rate (see Fig. 1). As a consequence, the difference in saturated energies between simulations with  $S_D = 0.01$  and references with  $S_D = 1$  differ by less than a factor of  $\sim 2$  over all of the investigated parameter space.

For the ICM, the estimated values are  $\beta \sim 10^2\text{--}10^4$  and  $\text{Kn}^{-1} \sim 10\text{--}100$  in the outskirts of galaxy clusters (Carilli & Taylor 2002; Vikhlinin et al. 2006). The physically relevant regime for

$\beta\text{Kn}$  is therefore  $\sim 1\text{--}10^3$ . Since simulations with small values of  $\text{Kn}_0^{-1}$  are computationally expensive (due to the time step constraint associated with thermal transport), we chose for practical reasons  $\text{Kn}_0^{-1} = 20 - 2 \times 10^4$ . This allowed us to perform very high resolution simulations for  $\text{Kn}_0^{-1} = 2000$ , a necessity for ensuring that our findings have numerically converged (see resolution study and

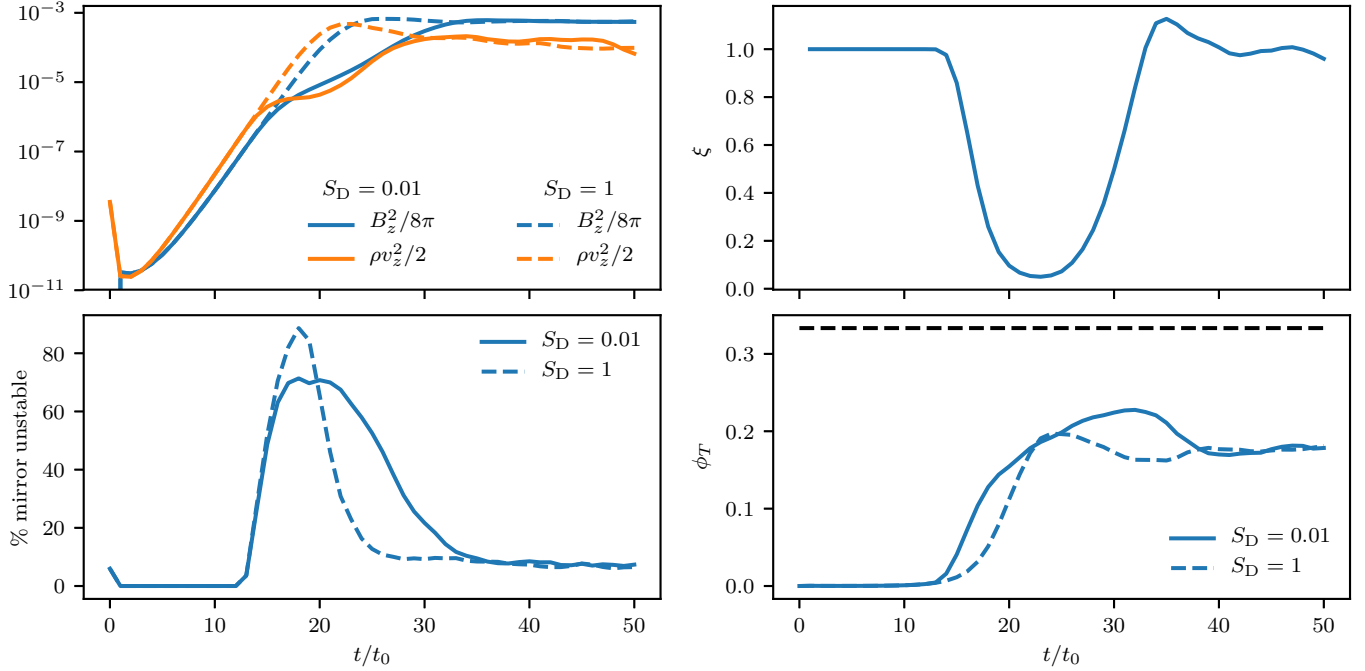


**Figure 5.** Time evolution in simulations of the MTI with  $S_D = 0.01$  (solid) and  $S_D = 1$  (dashed). Upper left: Vertical magnetic and kinetic energies. Upper right: Ratio of magnetic energy in the  $S_D = 0.01$  and  $S_D = 1$  simulations,  $\xi$ , defined in equation (21). Lower left: Mirror unstable volume fraction. Lower right: Normalized, magnetic field-aligned temperature gradient,  $\phi_T$ , defined in equation (22).

considerations in Appendix C). In order to capture the physically relevant regime for  $\beta \text{Kn} \sim 1\text{--}10^3$ , we increased the values for  $\beta_0$  as well, i.e.,  $\beta_0 = 10^4\text{--}10^7$  in the right-hand column of Fig. 6. Our initial conditions then cover the range  $\beta_0 \text{Kn}_0 = 5\text{--}5000$ . During the evolution of the simulation, the magnetic field strength is amplified by the MTI. This decreases the mean value of  $\beta$  such that the simulations with  $\beta_0 = 10^4\text{--}10^7$  at  $t/t_0 = 0$  have  $\beta = 10^{2.5}\text{--}10^{4.7}$  as the most frequent values at  $t/t_0 = 50$  (see Fig. 7). The simulations with  $\beta_0 = 10^5$  thus have  $\beta$  in the relevant range,  $\beta = 10^2\text{--}10^4$ , in more than 80 per cent of the MTI unstable domain at  $t/t_0 = 50$  (with 95 per cent for  $\beta_0 = 10^4$ ).

For the parameter scan, the important parameter for mirror instability,  $\beta_0 \text{Kn}_0$ , was chosen to be in the physically relevant range for the outskirts of galaxy clusters. And while we find modifications to the linear regime of the instability (i.e. decreased growth rates), differences are not present or are only moderate in the nonlinear regime. Thus over a factor of  $\sim 10^3$  in the product of thermal-to-magnetic pressure ratio,  $\beta_0$ , and collisionality measure,  $\text{Kn}_0$ , only a modest change to the saturation of the MTI is found by taking into account suppression of heat conductivity by the mirror instability.

### 3.6 3D simulations

We have so far only presented 2D simulations of the MTI, which are less computationally intensive than their more realistic 3D counterparts. The smaller computational cost allowed us to perform a parameter study at high numerical resolution in the previous section. In order to ensure that our findings are not an artifact of the reduced dimensionality, we also perform four 3D simulations. We consider the case  $\beta_0 = 10^5$  and  $\text{Kn}_0^{-1} = 2000$  only. Initially, the magnetic field is oriented along the  $x$ -direction and gravity acts in the negative  $z$ -direction. The extra dimensionality of the simulation now allows motions in the horizontal  $y$ -direction and all three velocity components are initialized with Gaussian noise.

We present a visualization of a simulation with  $S_D = 0.01$  at  $t/t_0 = 28$  in Fig. 8. Note that this figure shows the full computational domain, including the buffer regions used below and above the unstable region. The slices show pressure anisotropy and heat conductivity, respectively (compare with Fig. 4). The magnetic field lines display signatures of buoyant motions inside the central region.

We show the evolution of the volume average of the three magnetic energy components in a 3D simulation with  $S_D = 0.01$  (solid lines) and  $S_D = 1$  (dashed lines) in Fig. 9. As for the 2D simulation presented in Fig. 5, suppression of heat transport in mirror-unstable regions causes the growth rate to decrease. Nevertheless, the saturated energy levels are not changed by employing the subgrid model for heat transport described in Section 2.4.

As evident from Figs. 8 and 9, the motions are primarily in the  $z$ -direction and while a significant  $B_z$  component is created, the  $B_y$  component remains sub-dominant. This is likely the reason why we find the evolution of vertical magnetic energy in the  $S_D = 0.01$  and  $S_D = 1$  simulations to be almost identical to that in the 2D simulations (compare Figs. 5 and 9). That is, the saturation level of magnetic energy is the same in simulations with and without heat transport suppression, regardless of whether a 2D or a 3D study is performed. In addition, we find the same behavior for other diagnostics when comparing 2D and 3D simulations (such as the time-evolution of the mirror unstable fraction).

Finally, we study the time evolution of magnetic energy as a function of scale in the 3D simulations. Since the simulation domain is not periodic in  $z$ , we calculate  $|B(k)|^2$  in each horizontal slice of the unstable domain (here  $k = \sqrt{k_x^2 + k_y^2}$  is the horizontal wavenumber) and perform a vertical average in  $z$ . The resulting profiles are shown in Fig. 10 with blue (orange) lines at  $t = 28t_0$  and solid (dashed) lines obtained from simulations with  $S_D = 0.01$  ( $S_D = 1$ ). At  $t = 28t_0$  the simulation with suppression of heat conduction is lagging behind the reference simulation at all scales. The difference is most pronounced across large scales where heat

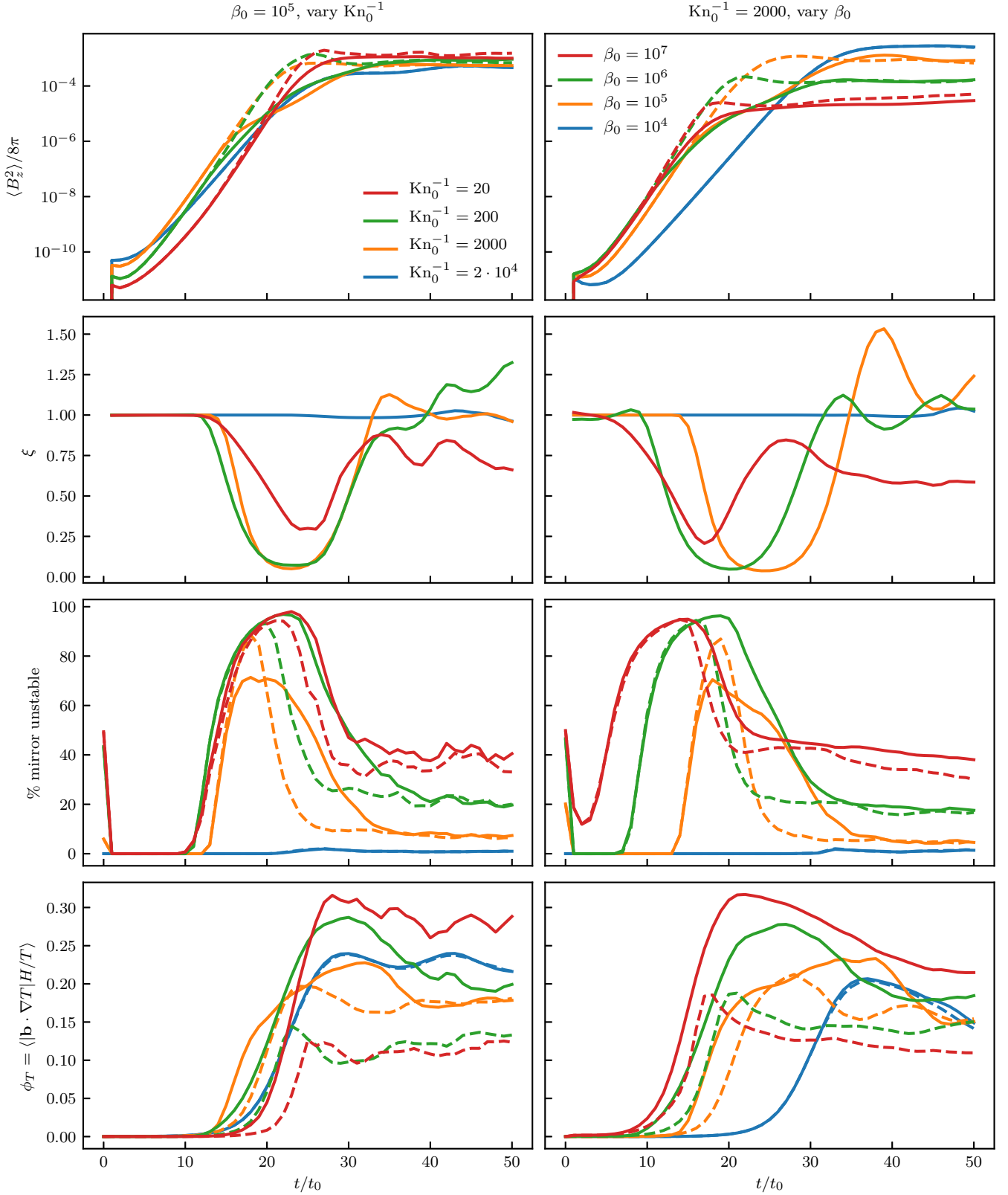


**Figure 6.** The effect of mirror-suppressed heat conductivity at various values of  $\beta_0$  and  $\text{Kn}_0^{-1}$ . We show the evolution of vertical magnetic energy (first row), ratio of magnetic energy in simulations with and without suppression,  $\xi$ , (second row, see equation 21), mirror-unstable fraction (third row) and field aligned temperature gradient,  $\phi_T$  (fourth row, see equation 22). Solid lines have suppression factor  $S_D = 0.01$  and dashed lines are reference simulations with  $S_D = 1$ . As expected from Equation 15, the mirror-unstable fraction is largest in the simulations with the largest  $\beta_0 \text{Kn}_0$  ( $\beta_0 \text{Kn}_0 = 5 \times 10^3$ , the red lines). These simulations thus have the largest regions with suppressed thermal conductivity and  $\phi_T$  becomes larger than in the simulations without suppression. Despite this change in conductivity, the final saturation energy of the MTI is ultimately only slightly modified. We interpret this latter observation using linear theory which, in the limit  $\beta_0 \text{Kn}_0 \gg 1$ , shows that the MTI growth rates remain significant even when the thermal conductivity is suppressed (see Fig. 1).



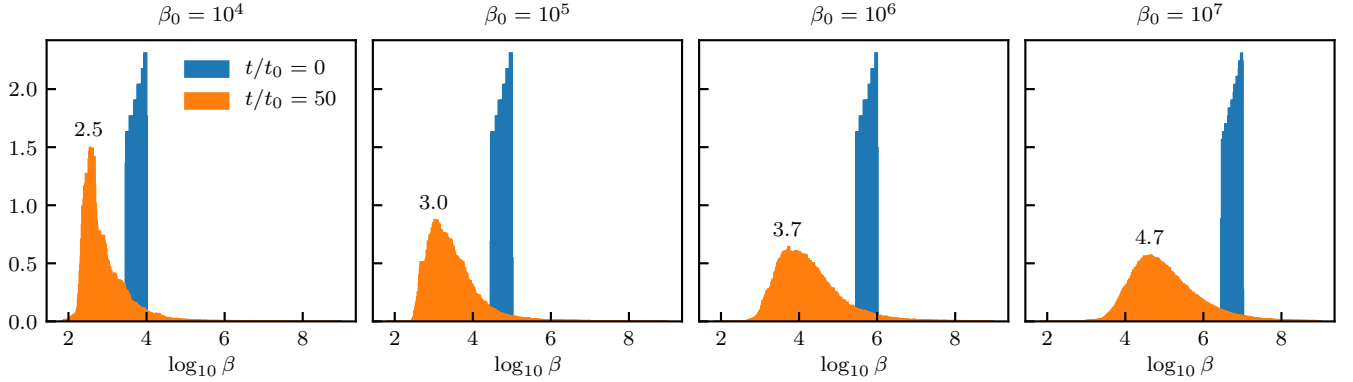


**Figure 7.** Distribution of  $\beta$  in the central, unstable part of the domain at  $t/t_0 = 0$  (blue) and  $t/t_0 = 50$  (orange) in simulations with different initial magnetic field strengths. The MTI increases the magnetic field strength and thus decreases  $\beta$ . The modes of the distributions are indicated at  $t/t_0 = 50$ .

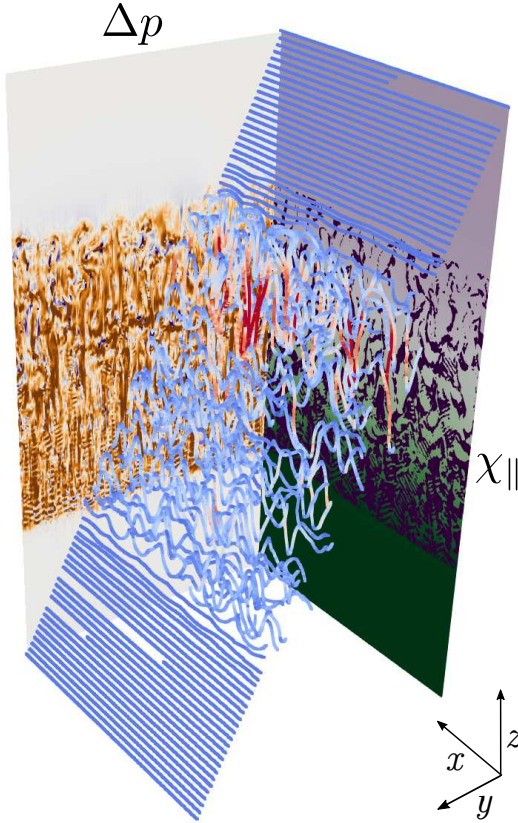


**Figure 8.** 3D MTI simulation with  $S_D = 0.01$  at  $t/t_0 = 28$ . The magnetic field lines are colored with red (blue) indicating higher (lower) magnetic field strength. The vertical slices show the pressure anisotropy,  $\Delta p$ , and the heat conductivity,  $\chi_{\parallel}$ . Mirror-unstable regions appear as purple patches in  $\chi_{\parallel}$ . See Fig. 4 for the 2D version.

conduction is more efficiently suppressed. At  $t = 50t_0$  this difference between the  $S_D = 0.01$  and  $S_D = 1$  simulations has however completely disappeared, and the simulations have the same energy both on large and small scales. The finding that the saturated state is insensitive to heat conduction suppression thus holds both in terms of volume-averaged energies (Fig. 9) and on a scale-by-scale basis (Fig. 10). The latter finding has importance for understanding how the MTI operates in combination with external turbulence. In particular, [McCourt et al. 2011](#) found that the MTI can maintain its power

spectrum on scales larger than the external driving scale even when strong external turbulence swamps out MTI turbulence on smaller scales (see their figure 14). Large scale MTI-driven motions thus survive both in simulations with external turbulence ([McCourt et al. 2011](#)) and in our simulations with  $S_D = 0.01$ . Understanding the combined influence of these two effects is outside the scope of the present work but we briefly discuss what could happen in Section 4.

In contrast to [McCourt et al. \(2011\)](#), [Ruszkowski et al. \(2011\)](#) studied the interaction between external turbulence and the MTI by performing cosmological simulations of cluster formation including anisotropic transport. They found little difference in radial bias of magnetic fields between simulations with and without anisotropic heat conduction. This could indicate that external turbulence suppresses the MTI. However, [Ruszkowski et al. \(2011\)](#) caution that *i*) it is difficult to disentangle the effect of the MTI and radial flow on the orientation of the magnetic fields *ii*) a systematic study of several galaxy clusters is required to make a definite statement regarding relative contributions of MTI/external turbulence as the ICM turbulence properties will differ from cluster to cluster. In addition, [McCourt et al. \(2011\)](#) show in their idealized setup that both external turbulence and the MTI lead to a randomization of the magnetic field orientation (see their figure 13). This makes volume integrated quantities poor diagnostics for determining the importance of the MTI. As such, a detailed understanding of whether the MTI is playing an active role in the simulations of [Ruszkowski et al. \(2011\)](#) might require spectral analysis such as the one performed by [McCourt et al. \(2011\)](#).

Numerical studies of turbulence in weakly collisional plasmas have so far been limited to idealized, turbulent box setups (e.g. [Squire et al. 2019](#); [Kempski et al. 2019](#)). Most notably [Squire et al. \(2019\)](#) have found that turbulence with Braginskii viscosity can display so-called *magneto-immutability*, i.e. that the turbulent motions are constrained to those that do not generate pressure anisotropy. While this pertains in particular to very viscous simulations without pressure anisotropy limiters (equation 12), even less viscous simulations with the limiters applied display a narrower distribution in the parallel rate-of-strain ( $bb : \nabla v$ , which in their incompressible simulations is directly proportional to  $\Delta p$ ). Of primary interest to the present work, the anisotropic viscous flux acts to reduce  $\Delta p$  and thus also the fraction of the volume which is unstable to the firehose and mirror instabilities (see figure 4 in [Squire et al. 2019](#)). Similar conclusions have been found in a study of the weakly collisional magnetic dynamo ([St-Onge et al. 2020](#), see in particular their appendix B 1 and figure 23) and in a study of turbulence driven by the



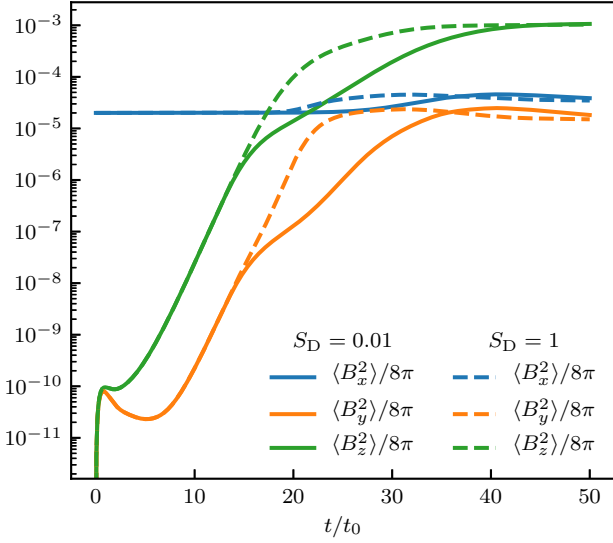


**Figure 9.** Evolution of magnetic energies in the 3D MTI simulation shown in Fig. 8. Numerical resolution is  $256 \times 256 \times 512$  and the same qualitative picture is found at resolution  $128 \times 128 \times 256$ .

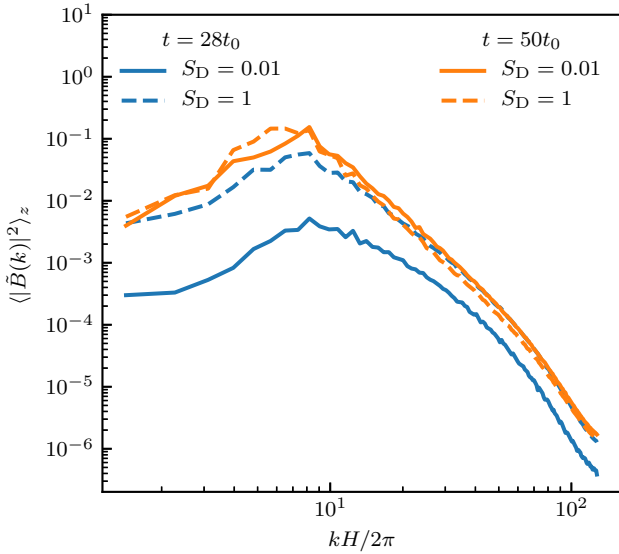


**Figure 10.** Magnetic field power spectrum averaged over the unstable domain. At  $t = 28t_0$ , the energy in the simulation with  $S_D = 0.01$  (solid blue line) lags behind the reference simulation with  $S_D = 1$  (dashed blue line), in particular on large scales across which heat conduction is suppressed at this point in time. At  $t = 50t_0$ , the power in the simulation including suppression by the mirror instability has caught up with the reference simulation on all scales (solid and dashed orange lines coincide).

magneto-rotational instability in weakly collisional accretion disk (Kempski et al. 2019, see their figure 9). The studies by Squire et al. (2019); St-Onge et al. (2020) considered incompressible turbulence using an Ornstein-Uhlenbeck process for the forcing term. Quantifying the mirror (and firehose) unstable fraction(s) in turbulence driven in a cosmological setting, i.e., where the turbulence is (at least weakly) compressible and driven by large-scale accretion and mergers has yet to be done and is an interesting avenue for future research.

#### 4 SUMMARY AND DISCUSSION

The MTI has been theorized to drive turbulence in the outer regions of galaxy clusters. In order to operate, the MTI requires fast heat conduction directed along the direction of the magnetic field (Balbus 2000, 2001). This type of anisotropic heat transport is expected in the ICM according to Braginskii (1965) because the high temperature and low density of the ICM makes Coulomb collisions rare. Particles are therefore expected to be effectively tied to the magnetic field, leading to transport of heat and momentum primarily along the field. This picture is muddled by various microscale instabilities which are not taken into account in the classical transport theory. PIC simulations show that microscale instabilities can create electromagnetic fluctuations that can scatter particles, effectively increasing the collision frequency and changing the heat transport properties of the plasma. In particular, Komarov et al. (2016) found that the ion mirror instability can suppress the heat conductivity by a factor  $S_D = 0.2$ . We use their results to motivate a subgrid model for the heat conductivity in Braginskii-MHD simulations. Our subgrid model is simple: In regions where the mirror instability threshold is exceeded,  $\Delta p/p > \beta^{-1}$ , we use a reduced heat conductivity,  $\chi_{\text{eff}} = S_D \chi_{\parallel}$ . Whereas Komarov et al. (2016) found  $S_D = 0.2$ , we have exaggerated mirror-suppression of heat transport by setting  $S_D = 0.01$  throughout the main body of the paper.

Since Braginskii-MHD simulations are less computationally intensive than PIC simulations, this subgrid method allows us to perform simulations that model a larger spatial extent of the ICM compared to what would be possible with PIC simulations. Using this approach, we perform a series of simulations of the MTI in both 2D (Sections 3.3, 3.4 and 3.5) and 3D (Section 3.6). In these simulations, the MTI grows exponentially until its amplitude is large enough to exceed the threshold for stability of the mirror instability. When this occurs, the heat conductivity is suddenly dramatically reduced in a large volume of the system. One would naively expect this to quench the MTI which depends on efficient heat transport along magnetic field lines. However, this intuition turns out to be wrong and we have found surprisingly small effects on the evolution of the MTI.

We explain this behavior as follows: Whether the mirror instability is active in large regions of the simulation depends on the value of  $\beta_0 \text{Kn}_0$  where  $\beta_0$  is the ratio of thermal to magnetic pressure and  $\text{Kn}_0$  is the Knudsen number (see Section 2.2). When  $\beta_0 \text{Kn}_0 = 5$ , the MTI-generated motions are not sufficient to excite the mirror-instability, while it is excited when  $\beta_0 \text{Kn}_0 = 5000$  (see Fig. 6). The associated heat transport suppression does not, however, quench the MTI in the latter case because heat conduction remains fast even after suppression when  $\beta_0 \text{Kn}_0 = 5000$ . We show this by calculating the MTI growth rates using linear theory in Section 3.2, see Fig. 1.

In summary, when  $\beta_0 \text{Kn}_0$  is small, the mirror-instability does not modify the MTI-evolution (simply because it is not active) and when  $\beta_0 \text{Kn}_0$  is large, the MTI is so far into the fast heat conduction regime, that suppression of the thermal conductivity, even by a factor  $S_D = 0.01$ , is insufficient to severely limit its growth rate. For a range of values of  $\text{Kn}_0^{-1}$  and  $\beta$ , the evolution of the MTI therefore appears to be quite robust to reductions of the heat conductivity by the mirror instability. And while we do not find a large effect on the MTI evolution when  $S_D = 0.01$  and  $\beta_0 \text{Kn}_0$  is large, the effect becomes even smaller when the value inferred by Komarov et al. (2016),  $S_D = 0.2$ , is used. This is illustrated in Fig. 11 where we compare simulations with  $S_D = 0.01, 0.2$  and 1 and find almost identical evolution for  $S_D = 0.2$  and 1.

There are, however, limitations to the present study. First, we

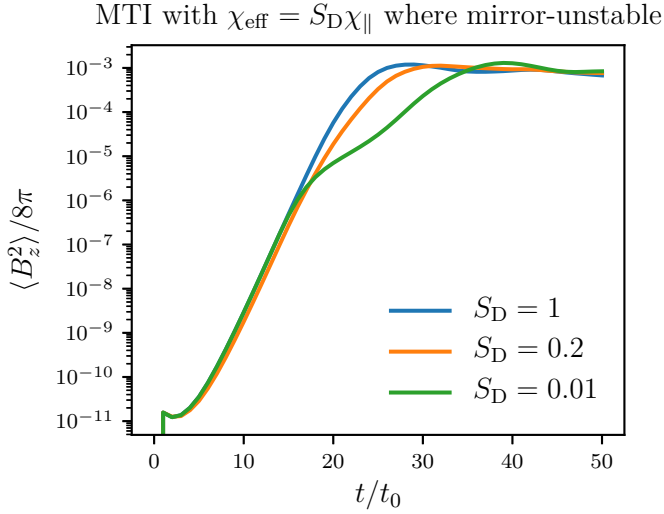


**Figure 11.** Evolution of energies in simulations with varying suppression factor,  $S_D$ , at fixed  $\text{Kn}_0^{-1} = 2000$  and  $\beta_0 = 10^5$ . The growth rate of the MTI is reduced in the simulations with  $S_D < 1$  but the saturated energies are not.

have only considered plasma motions generated by the MTI itself. This yields an interesting dynamical system with negative feedback, i.e., fast heat transport drives vigorous plasma motions, which suppress the heat transport, which then only drives weaker motions and allows the heat transport to again increase (thus closing the loop). It is however important to mention that several other mechanisms generate plasma motions and associated pressure-anisotropy, e.g., AGN and merger-driven motions (Zuhone et al. 2011; McNamara & Nulsen 2012; Kannan et al. 2017; Barnes et al. 2019). It is not clear how (and if) a suppression of heat transport will modify these large-scale phenomena. Such external turbulence (in addition to the turbulence driven by the MTI itself) could also modify the MTI evolution by randomizing magnetic field lines (Ruszkowski et al. 2011; McCourt et al. 2011). McCourt et al. (2011) investigated this and found that the MTI is able to drive strong turbulence even in the presence of external turbulence. In particular, they found that the MTI persists on scales larger than the injection scale of the external turbulence. McCourt et al. (2011) did however not include Braginskii viscosity and suppression of heat conductivity. If the conductivity is suppressed in mirror unstable regions, then the external turbulence could also modify the MTI by driving positive pressure anisotropy and creating mirror unstable regions. Driven turbulence in incompressible, weakly collisional plasmas is under active investigation (Santos-Lima et al. 2014; Squire et al. 2019; St-Onge et al. 2020). While these idealized studies find that a large fraction of the volume is mirror unstable the mirror unstable volume fraction in turbulence driven by gas accretion and mergers in galaxy clusters is not well-known. Alfvénic turbulence with Braginskii viscosity driven via an Ornstein-Uhlenbeck process shows that weakly collisional systems will have smaller parallel rate-of-strain,  $\mathbf{b}\mathbf{b}:\nabla\mathbf{v}$ , than found in ideal MHD (Squire et al. 2019). This tendency, termed *magneto-immutability*, means that one cannot simply obtain  $\Delta p$  by post-processing a cosmological simulation performed with ideal MHD and anisotropic conduction (such as the one by Ruszkowski et al. 2011). While a detailed understanding of the mirror-unstable fraction in a more realistic, cosmological setting thus awaits further work, we note for now that we have found that the saturated state of the MTI in our setup is rather insensitive to suppression of heat conductivity over a large range in  $\beta_0\text{Kn}_0$  even

when the mirror unstable fraction is substantial (see Fig. 6). Taken in combination with the results of McCourt et al. (2011), this indicates that a study with external turbulence and  $S_D = 0.01$  would find slower growth of the MTI already at the onset of the simulation but that the nonlinear saturation state would be very similar to the one found in simulations without turbulence and heat conduction suppression. Testing this prediction will require a dedicated study taking both heat conduction suppression and external turbulence into account.

In terms of microphysics, a major limitation of our study is that our subgrid model for heat conduction considers suppression of heat conductivity by the ion mirror instability only. Another important candidate for suppression of heat conductivity is the electron whistler instability (Komarov et al. 2014; Roberg-Clark et al. 2016, 2018a,b; Komarov et al. 2018; Riquelme et al. 2018). This instability could also modify the dynamics and vigorousness of the MTI. Importantly, while our subgrid model couples the efficiency of heat transport to plasma motions (via the rate-of-strain tensor and local magnetic field), suppression by the whistler instability can depend directly on the gradient in temperature. This occurs because the whistler instability is driven unstable by the temperature gradient itself (Komarov et al. 2018). Whether the MTI survives when taking this effect into account is likely to be the topic of future research (e.g. Drake et al. 2020). Another complication is that the MTI itself also exists in the collisionless regime (Xu & Kunz 2016). Their linear analysis for a thermally stratified, magnetized and collisionless plasma showed that the kinetic variant of the MTI also has an electron counterpart. The electron MTI (eMTI) can grow faster than the standard MTI (Xu & Kunz 2016). It is however not clear how the eMTI saturates and whether it modifies subsequent heat transport. The final conclusion could therefore potentially involve the outcome of a competition between the eMTI and the electron whistler instability driven unstable by a thermal gradient.

The goal of our study was to understand whether the MTI is modified by the mirror instability. In a broader context, however, the motivation was also to understand whether we can reliably include kinetic effects as subgrid models in fluid simulations. The MTI here serves as an interesting testbed, as future PIC simulations could potentially study the collisionless MTI (Xu & Kunz 2016) in a local 2D setup (Parrish & Stone 2005). As global galaxy cluster simulations using PIC are inconceivable in the foreseeable future, it will inevitably be necessary to include kinetic effects via subgrid prescriptions. Here we propose using the MTI, an interesting yet somewhat simple dynamical system where the microscales drive the macroscales (and vice versa), as a stepping stone.

## ACKNOWLEDGMENTS

We thank the anonymous referee for constructive reports with valuable comments on plasma physics and the role of external turbulence. This work was initiated during an extended research stay by TB at the Theoretical Astrophysics Center (TAC), University of California, Berkeley, and TB thanks TAC for hosting him. TB and MEP acknowledge support by the European Research Council under the European Union’s Seventh Framework Programme (FP/2007-2013) under ERC grant agreement 306614. TB and CP acknowledge support by the European Research Council under ERC-CoG grant CRAGSMAN-646955. This work was supported in part by a Simons Investigator Award from the Simons Foundation (EQ). This research was supported in part by the National Science Foundation under Grant No. NSF PHY-1748958. Our data analysis and plot-

ting was performed with Python (Van Rossum & Drake 2009) using Numpy (van der Walt et al. 2011), Scipy (Virtanen et al. 2020) and Matplotlib (Hunter 2007). We thank the developers for making these tools freely available.

## DATA AVAILABILITY

The data underlying this article will be shared on reasonable request to the corresponding author. The data was generated with a modified version of the Athena code, publicly available at <https://princetonuniversity.github.io/Athena-Cversion/>.

## REFERENCES

- Balbus S. A., 2000, *ApJ*, **534**, 420
- Balbus S. A., 2001, *ApJ*, **562**, 909
- Bale S. D., Kasper J. C., Howes G. G., Quataert E., Salem C., Sundkvist D., 2009, *Physical Review Letters*, **103**, 211101
- Barnes D. J., et al., 2019, *MNRAS*, **488**, 3003
- Berlok T., Pessah M. E., 2015, *ApJ*, **813**, 22
- Berlok T., Pessah M. E., 2016a, *ApJ*, **824**, 32
- Berlok T., Pessah M. E., 2016b, *ApJ*, **833**, 164
- Berlok T., Pfrommer C., 2019, *MNRAS*, **485**, 908
- Berlok T., Pakmor R., Pfrommer C., 2019, *MNRAS*, **p. 2732**
- Birdsall C. K., Langdon A. B., 1991, *Plasma Physics via Computer Simulation*
- Braginskii S., 1965, *Review of Plasma Physics*
- Brown B. P., Vasil G. M., Zweibel E. G., 2012, *ApJ*, **756**, 109
- Carilli C. L., Taylor G. B., 2002, *ARA&A*, **40**, 319
- Chandrasekhar S., Kaufman A. N., Watson K. M., 1958, *Proceedings of the Royal Society of London Series A*, **245**, 435
- Chen C. H. K., Matteini L., Schekochihin A. A., Stevens M. L., Salem C. S., Maruca B. A., Kunz M. W., Bale S. D., 2016, *ApJ*, **825**, L26
- Drake J. F., Pfrommer C., Reynolds C. S., Ruszkowski M., Swisdak M., Einarsson A., Hassam A. B., Roberg-Clark G. T., 2020, *arXiv e-prints*, **p. arXiv:2007.07931**
- Gary S. P., 1993, *Theory of Space Plasma Microinstabilities*
- Hasegawa A., 1969, *Physics of Fluids*, **12**, 2642
- Hockney R. W., Eastwood J. W., 1988, *Computer simulation using particles*
- Hunter J. D., 2007, *Computing in Science & Engineering*, **9**, 90
- Ichimaru S., 1973, *Basic principles of plasma physics: a statistical approach*. Benjamin/Cummings Publishing Company
- Kannan R., Vogelsberger M., Pfrommer C., Weinberger R., Springel V., Hernquist L., Puchwein E., Pakmor R., 2017, *ApJ*, **837**, L18
- Kempki P., Quataert E., Squire J., Kunz M. W., 2019, *MNRAS*, **486**, 4013
- Kempki P., Quataert E., Squire J., 2020, *MNRAS*, **493**, 5323
- Komarov S. V., Churazov E. M., Schekochihin A. A., Zuhone J. A., 2014, *MNRAS*, **440**, 1153
- Komarov S. V., Churazov E. M., Kunz M. W., Schekochihin A. A., 2016, *MNRAS*, **460**, 467
- Komarov S., Schekochihin A. A., Churazov E., Spitkovsky A., 2018, *Journal of Plasma Physics*, **84**, 905840305
- Krall N. A., Trivelpiece A. W., 1973, *Principles of plasma physics*. McGraw-Hill, New York
- Kulsrud R. M., 1983, in Galeev A. A., Sudan R. N., eds, *Basic Plasma Physics: Selected Chapters, Handbook of Plasma Physics*, Vol. 1. p. 1
- Kunz M. W., 2011, *MNRAS*, **417**, 602
- Kunz M. W., Bogdanović T., Reynolds C. S., Stone J. M., 2012, *ApJ*, **754**, 122
- Kunz M. W., Schekochihin A. A., Stone J. M., 2014, *Physical Review Letters*, **112**, 205003
- Kunz M. W., Squire J., Schekochihin A. A., Quataert E., 2020, *arXiv e-prints*, **p. arXiv:2006.08940**
- Latter H. N., Kunz M. W., 2012, *MNRAS*, **423**, 1964
- Lesur G., 2015, *Snoopy: General purpose spectral solver (ascl:1505.022)*
- McCourt M., Parrish I. J., Sharma P., Quataert E., 2011, *MNRAS*, **413**, 1295
- McNamara B. R., Nulsen P. E. J., 2012, *New Journal of Physics*, **14**, 055023
- Meyer C. D., Balsara D. S., Aslam T. D., 2012, *MNRAS*, **422**, 2102
- Parker E. N., 1958, *Physical Review*, **109**, 1874
- Parrish I. J., Stone J. M., 2005, *ApJ*, **633**, 334
- Parrish I. J., Stone J. M., 2007, *ApJ*, **664**, 135
- Parrish I. J., Stone J. M., Lemaster N., 2008, *ApJ*, **688**, 905
- Parrish I. J., McCourt M., Quataert E., Sharma P., 2012a, *MNRAS*, **419**, L29
- Parrish I. J., McCourt M., Quataert E., Sharma P., 2012b, *MNRAS*, **422**, 704
- Pessah M. E., Chakraborty S., 2013, *ApJ*, **764**, 13
- Quataert E., 2008, *ApJ*, **673**, 758
- Riquelme M. A., Quataert E., Verscharen D., 2016, *ApJ*, **824**, 123
- Riquelme M., Quataert E., Verscharen D., 2018, *ApJ*, **854**, 132
- Roberg-Clark G. T., Drake J. F., Reynolds C. S., Swisdak M., 2016, *ApJ*, **830**, L9
- Roberg-Clark G. T., Drake J. F., Reynolds C. S., Swisdak M., 2018a, *Physical Review Letters*, **120**, 035101
- Roberg-Clark G. T., Drake J. F., Swisdak M., Reynolds C. S., 2018b, *ApJ*, **867**, 154
- Ruszkowski M., Lee D., Brüggemann M., Parrish I., Oh S. P., 2011, *ApJ*, **740**, 81
- Santos-Lima R., de Gouveia Dal Pino E. M., Kowal G., Falceta-Gonçalves D., Lazarian A., Nakwacki M. S., 2014, *ApJ*, **781**, 84
- Schekochihin A. A., Cowley S. C., 2006, *Astronomische Nachrichten*, **327**, 599
- Schekochihin A. A., Cowley S. C., Kulsrud R. M., Hammett G. W., Sharma P., 2005, *ApJ*, **629**, 139
- Schekochihin A. A., Cowley S. C., Rincon F., Rosin M. S., 2010, *MNRAS*, **405**, 291
- Schwarzschild M., 1958, *Structure and Evolution of the Stars*.
- Sharma P., Hammett G. W., 2007, *Journal of Computational Physics*, **227**, 123
- Sharma P., Hammett G. W., Quataert E., Stone J. M., 2006, *ApJ*, **637**, 952
- Spiegel E. A., Veronis G., 1960, *ApJ*, **131**, 442
- Spitzer L., 1962, *Physics of Fully Ionized Gases*
- Squire J., Quataert E., Schekochihin A. A., 2016, *ApJ*, **830**, L25
- Squire J., Schekochihin A. A., Quataert E., 2017a, *New Journal of Physics*, **19**
- Squire J., Kunz M. W., Quataert E., Schekochihin A. A., 2017b, *Phys. Rev. Lett.*, **119**, 155101
- Squire J., Schekochihin A. A., Quataert E., Kunz M. W., 2019, *Journal of Plasma Physics*, **85**, 905850114
- St-Onge D. A., Kunz M. W., Squire J., Schekochihin A. A., 2020, *arXiv e-prints*, **p. arXiv:2003.09760**
- Stix T. H., 1992, *Waves in Plasmas*. American Institute of Physics, New York
- Stone J. M., Gardiner T., 2009, *New Astronomy*, **14**, 139
- Stone J. M., Gardiner T. A., Teuben P., Hawley J. F., Simon J. B., 2008, *ApJ Supplement Series*, **178**, 137
- Swanson D. G., 1989, *Plasma waves*.
- Vaidya B., Prasad D., Mignone A., Sharma P., Rickler L., 2017, *MNRAS*, **472**, 3147
- Van Rossum G., Drake F. L., 2009, *Python 3 Reference Manual*. CreateSpace, Scotts Valley, CA
- Vasil G. M., Lecoanet D., Brown B. P., Wood T. S., Zweibel E. G., 2013, *ApJ*, **773**, 169
- Vikhlinin A., Kravtsov A., Forman W., Jones C., Markevitch M., Murray S. S., Van Speybroeck L., 2006, *ApJ*, **640**, 691
- Virtanen P., et al., 2020, *Nature Methods*, **17**, 261
- Xu R., Kunz M. W., 2016, *Journal of Plasma Physics*, **82**, 905820507
- Zuhone J. A., Markevitch M., Lee D., 2011, *ApJ*, **743**, 16
- Zweibel E. G., Mirnov V. V., Ruszkowski M., Reynolds C. S., Yang H. Y. K., Fabian A. C., 2018, *ApJ*, **858**, 5
- van der Walt S., Colbert S. C., Varoquaux G., 2011, *Computing in Science Engineering*, **13**, 22

## APPENDIX A: WAVE DISRUPTION BY SUPPRESSION OF HEAT CONDUCTION

In this appendix, we analyze how sound waves are modified when the heat conductivity is suppressed in mirror unstable regions. Our analysis is a fluid analogue of the kinetic analysis and simulations of Kunz et al. (2020). Sound waves decay via thermal conduction and viscosity, and their decay rate is expected to change if the heat conductivity is suppressed. At the same time, sound waves themselves generate pressure anisotropy (via density changes, see equation 8), and sound waves with sufficiently high amplitude can exceed the mirror instability threshold. The resulting suppression of thermal conductivity is not uniform across the wave, and results in a complicated modification to the waveform. Here we illustrate the modified wave evolution by using a simple one-dimensional (1D) setup.

We consider a longitudinal sound wave with small variations in the temperature,  $\delta T$ , density,  $\delta \rho$ , and velocity,  $\mathbf{v} = \delta v \mathbf{e}_x$ . A background magnetic field,  $\mathbf{B} = B \mathbf{e}_x$ , sets the direction of anisotropic transport but does not directly enter the dynamics. The domain is periodic with length  $L$  in the  $x$ -direction. The system can be modeled with the following set of linearized equations<sup>7</sup>

$$\frac{\partial}{\partial t} \frac{\delta \rho}{\rho} = -\frac{\partial \delta v}{\partial x}, \quad (\text{A1})$$

$$\frac{\partial \delta v}{\partial t} = -\frac{1}{\rho} \frac{\partial \delta p}{\partial x} + \frac{2}{3\rho} \frac{\partial \delta \Delta p}{\partial x}, \quad (\text{A2})$$

$$\frac{\partial}{\partial t} \frac{\delta T}{T} = -(\gamma - 1) \frac{\partial \delta v}{\partial x} + \frac{(\gamma - 1)}{p} \frac{\partial}{\partial x} \left( \chi_{\parallel} \frac{\partial \delta T}{\partial x} \right), \quad (\text{A3})$$

where the pressure anisotropy is given by

$$\delta \Delta p = -2\nu_{\parallel} \frac{d\delta \rho}{dt} = 2\rho\nu_{\parallel} \frac{\partial \delta v}{\partial x}. \quad (\text{A4})$$

Here, the effects of anisotropic heat conduction and Braginskii viscosity are included via the coefficients  $\chi_{\parallel}$  and  $\nu_{\parallel}$ . We expect both of these effects to lead to damping of the wave (due to diffusion of temperature and velocity, respectively).

Fluctuations with sufficiently high amplitude violate the mirror instability threshold, equation (14), and lead to a reduction in the effective viscosity and heat conductivity. Building on earlier work by Squire et al. 2016; Squire et al. 2017a,b for Alfvén waves, this effect has very recently been studied for a collisionless system (Kunz et al. 2020). For sufficiently small amplitude fluctuations (such that  $\Delta p < B^2/8\pi$  at all times, see detailed criterion below), solutions can however be adequately described with linear theory. We find that the system of equations given by Equations (A1)–(A4) yields the eigenvalue problem

$$\begin{pmatrix} -\omega & kc & 0 \\ kc & -i\frac{4}{3}\nu_{\parallel}k^2 - \omega & kc \\ 0 & (\gamma - 1)kc & -i\frac{\gamma - 1}{p}\chi_{\parallel}Tk^2 - \omega \end{pmatrix} \begin{pmatrix} \delta \rho / \rho \\ \delta v / c \\ \delta T / T \end{pmatrix} = 0, \quad (\text{A5})$$

when Fourier transformed in time and space, assuming that  $\chi_{\parallel}$  and  $\nu_{\parallel}$  are constant. Solutions to equation (A5) show that acoustic waves decay at an exponential rate due to both heat conduction and Braginskii viscosity. Since heat conduction acts on a faster

time scale than viscosity (see equation 11), heat conduction is the dominant effect in the decay of such low amplitude waves.

The linear analysis breaks down if the mirror threshold is passed (i.e. if equation 14 is satisfied). Whether the heat conductivity is reduced due to the pressure anisotropy generated by the wave, thus depends on the amplitude of the sound wave. Using the linear solution for the evolution of pressure anisotropy, and ignoring the detailed time and space dependence, the heat conductivity is reduced if

$$2\rho\nu_{\parallel}k|A|c \gtrsim \frac{B^2}{8\pi}, \quad (\text{A6})$$

where  $A c$  is the initial amplitude of the velocity perturbation. In terms of the dimensionless quantities  $\beta$ ,  $\text{Kn}^{-1}$  and  $kL$ , the limit is therefore predicted to be

$$|A| \gtrsim \frac{\text{Kn}^{-1}}{\beta kL}. \quad (\text{A7})$$

Equation (A7) shows that the sound wave itself most effectively suppress the heat conductivity when the magnetic field is weak (i.e. when  $\beta$  is large) or when collisions are rare (i.e. when  $\text{Kn}^{-1}$  is small). Additionally, interruption occurs more easily for short wavelength waves (i.e. large wavenumbers,  $kL$ ).

We solve equations (A1)–(A4) numerically<sup>8</sup> in order to understand how the wave evolution is modified when the initial amplitude exceeds the limit given by equation (A7). The simulations are initialized with an acoustic wave solution obtained<sup>9</sup> from the eigenvalue problem given by equation (A5), i.e.,  $\delta v/c = A \cos(kx)$ ,  $\delta \rho/\rho = A_{\rho} \sin(kx)$ , and  $\delta T/T = A_T \sin(kx)$  where  $A$ ,  $A_{\rho}$  and  $A_T$  are dimensionless amplitudes. The linear solution is then a decaying, standing wave with frequency  $\omega = \omega_0 + i\Gamma$  where  $\omega_0$  is the oscillation frequency and  $\Gamma$  is the decay rate.

We show an example of modified wave evolution in Fig. A1, with the simulation (solid lines) and the small-amplitude linear theory for comparison (dashed lines). The simulation has  $kL = 2\pi$ ,  $\beta = 2 \times 10^4$  and  $\text{Kn}^{-1} = 200$  (here defined as  $\text{Kn} = \lambda_i/L$ ). These parameters yield  $\text{Kn}^{-1}/(\beta kL) = 1.6 \times 10^{-3}$  which is less than the initial velocity amplitude ( $|A| = 7.3 \times 10^{-3}$ ). This consequently leads to suppression of heat conductivity by a factor  $S_D = 0.01$  in the mirror-infested regions which are indicated with orange solid lines. Due to the suppressed conductivity, temperature fluctuations decay at a much slower rate in the mirror-infested regions than in the regions unaffected by the mirror instability. This leads to a terraced structure in temperature with steep slopes in temperature occurring where the conductivity is suppressed and shallow slopes occurring where the unsuppressed conductivity quickly erases temperature fluctuations (see in particular the third panel in Fig. A1). Note that this modification of the wave structure depends on the applied suppression factor,  $S_D$ . For instance, the modification is less dramatic when the value motivated by Komarov et al. (2016),  $S_D = 0.2$ , is used. High-frequency variation in the heat conductivity is however still found to sporadically occur in sound wave and MTI simulations with  $S_D = 0.2$  (see the online supplementary material).

<sup>8</sup> The numerical solutions are found with a fast Fourier transform (FFT) method for the spatial derivatives and a fourth order Runge-Kutta time step procedure. We additionally apply a sixth order hyper-viscosity term to  $\delta \rho$ ,  $\delta v$  and  $\delta T$  to avoid buildup of grid scale noise.

<sup>9</sup> Three solutions are found: a decaying solution with zero real frequency,  $\omega_0 = 0$ , as well as two waves traveling to the left and right, respectively. The standing wave solution used for initializing simulations is constructed from the two traveling waves.

<sup>7</sup> We assume equal ion and electron temperatures for direct comparison with our study of the MTI. Note, however, that this approximation is expected to break down for sound waves which vary on a fast time scale compared to the ion-electron equilibration time scale (see e.g. Zweibel et al. 2018; Kempfski et al. 2020 for a detailed discussion of this).



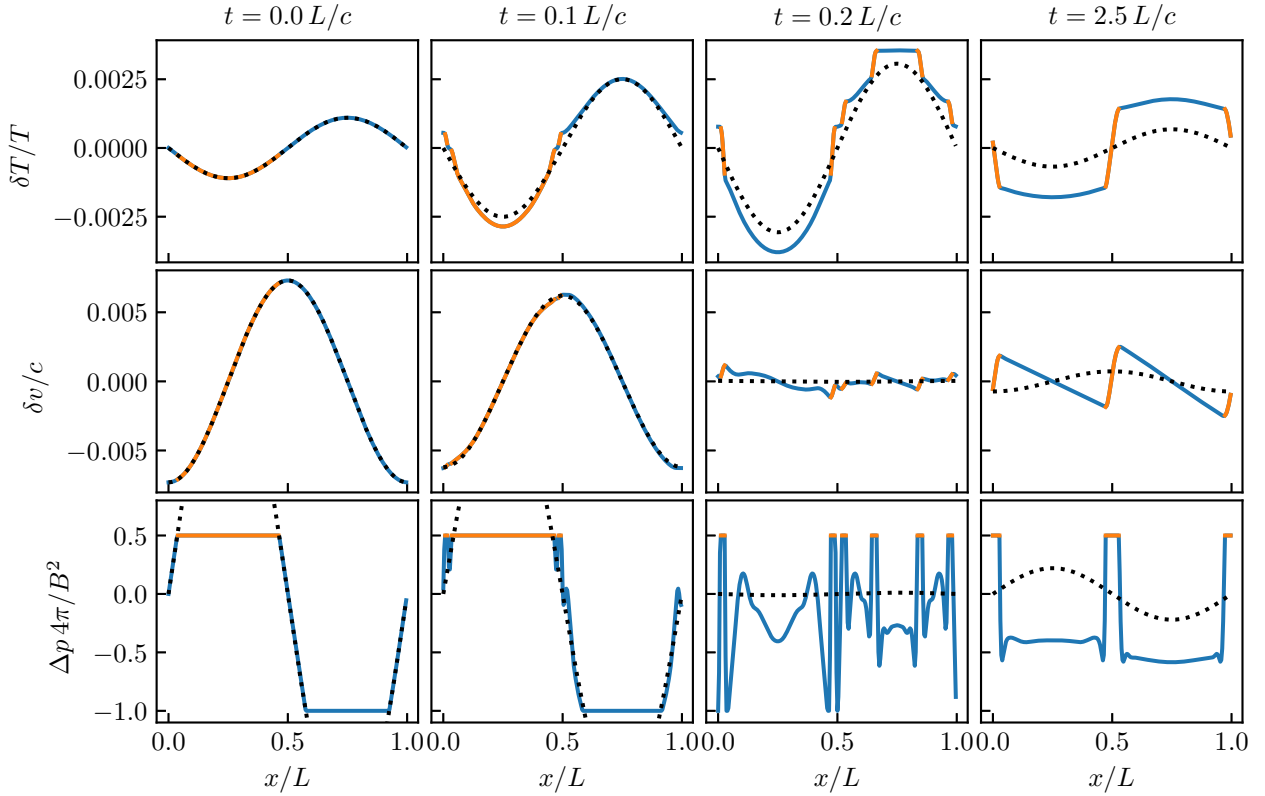


**Figure A1.** Evolution of an acoustic wave in Braginskii-MHD with a subgrid model for suppression of heat conductivity (which mimicks reduction by the mirror instability, see Section 2.3). Dotted lines show small-amplitude solutions to equation (A5). Solid lines are a numerical solution obtained with FFT methods. Orange regions have surpassed the mirror threshold, equation (14), and the heat conductivity is reduced by a factor  $S_D = 0.01$  in these regions. The decay of temperature fluctuations is consequently much slower in these regions and the temperature distribution becomes terraced (upper row). The pressure anisotropy (lower row) has a high frequency component which depends on the grid scale.

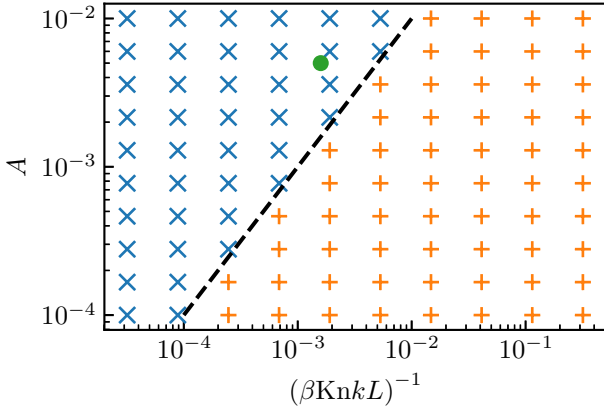


**Figure A2.** Numerical simulations with various initial amplitudes,  $A$ , and interruption parameters,  $(\beta KnkL)^{-1}$ . Data points located above the dashed line, given by equation (A7), exceeded the threshold for instability and had suppressed heat conductivity. The solid green circle corresponds to the parameters that were used for the simulation presented in Fig. A1.

The numerical simulation in Fig. A1 shows that suppression of heat conductivity in mirror-unstable regions can delay the wave decay. In Fig. A2 we compare our analytical prediction for when this interruption of acoustic waves occurs, equation (A7), with results from a suite of simulations where we varied the wave amplitude,  $A$ , and the magnetic field strength,  $\beta$ . In this figure, blue crosses indicate simulations in which the mirror stability threshold was violated and the wave evolution was modified by mirror instability-induced

suppression of the heat conductivity. Below the amplitude-threshold given by equation (A7), orange plus signs indicate simulations in which the mirror instability threshold was not violated and the wave evolution decayed in agreement with simple linear theory.

A limitation of our subgrid model is that sound waves are more likely to trigger the mirror instability at high wavenumber (small spatial scales, see equation A7). This causes a grid-scale dependence in the suppression of heat conductivity (i.e. the striations seen in Fig. 2). Despite this grid-scale dependence, our simulations reach the same result (that the MTI perseveres despite the suppression of thermal conductivity) at several different levels of numerical grid resolution (see Appendix C). Nevertheless, it would be beneficial to construct a regularization method which sets a minimum length scale for regions with suppressed conductivity. A well motivated regularization method could perhaps be informed from collisionless theory or simulations. The mirror instability creates fluctuations in the magnetic field with a correlation length of  $\sim 100 - 200 \rho_i$  where  $\rho_i$  is the ion Larmor radius (Komarov et al. 2016). On smaller scales, the suppression of heat conduction is no longer efficient, see figure 5 in Komarov et al. (2016). This means that our subgrid model for heat conductivity should be modified at small spatial scales below which the heat conductivity is not expected to be effectively suppressed. While these scales are much too small to be resolved in our simulations, one could artificially increase the cutoff scale in order for it to be resolvable. Such a regularization method would then remove the grid-scale dependence of the characteristic size of mirror-infested regions. Alternatively, one could use an incompressible code, such as snoopy (Lesur 2015), to solve the Boussinesq equations and thereby eliminate sound waves from the simulation.

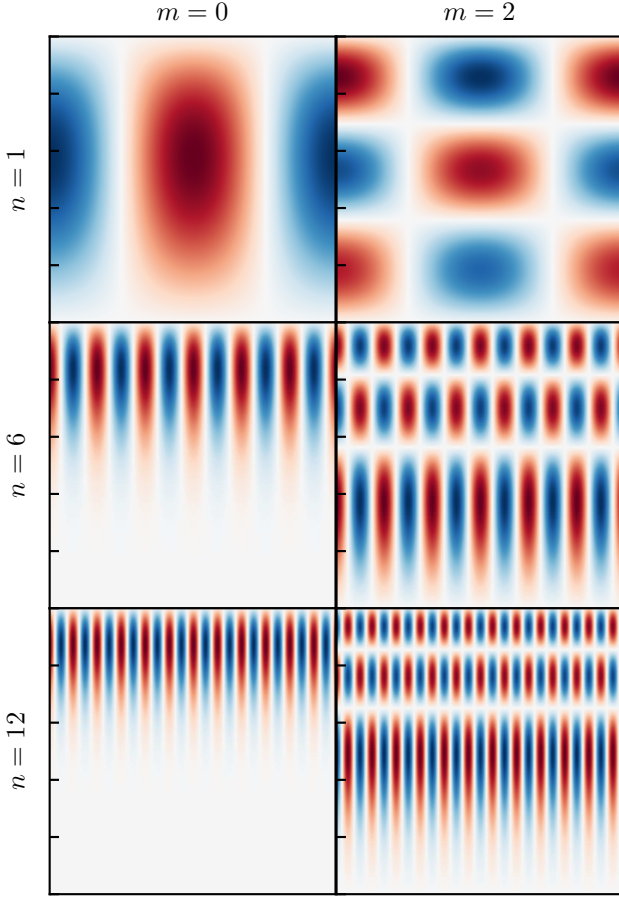


**Figure B1.** The  $\delta v_z$  component of eigenmodes obtained for  $k_{\parallel}H = 2\pi n$  where  $n = 1, 6$  and  $12$  are the horizontal mode numbers and  $m = 0$  and  $2$  are the vertical mode numbers.

However, while the local, linear theory of the MTI can be derived in the Boussinesq approximation, [McCourt et al. \(2011\)](#) showed that local simulations underestimate the saturation amplitude of turbulent motions compared to a larger box where the vertical extent is not much smaller than the scale height. Such a quasi-global setup, which we also use in our work, is at odds with the Boussinesq approximation which assumes  $L_z \ll H$  (e.g. [Spiegel & Veronis 1960](#)). To get around this limitation of the Boussinesq approximation, one could instead employ alternative so-called sound-proof equation sets such as the anelastic approximation or a pseudo incompressible model (see [Brown et al. 2012](#), [Vasil et al. 2013](#) and references therein for a thorough discussion of these methods for modeling low Mach number, stratified atmospheres). In addition, the Mach number,  $\mathcal{M} = |v|/(\sqrt{\gamma}c)$ , in our non-linear simulations saturate with a root-mean-square (RMS) value  $\mathcal{M}_{\text{rms}} \sim 10^{-2}$  with the largest values reaching  $\mathcal{M}_{\text{max}} \sim 0.1$ . For this reason, modeling the MTI in a local Boussinesq approximation or a pseudo-incompressible model which assumes  $\mathcal{M} \ll 1$  would come with other limitations. We leave investigating these issues further to future work.

## APPENDIX B: QUASI-GLOBAL, LINEAR THEORY FOR THE MTI

Equations (2)–(5) are linearized around the equilibrium given in Section 3.1. The perturbations are assumed to have the form

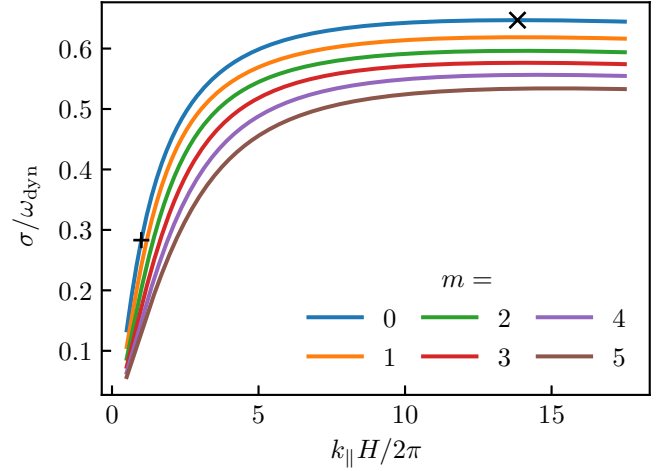


**Figure B2.** Growth rates as a function of the two mode numbers  $n = k_{\parallel}H/2\pi$  and  $m$  using quasi-global theory. The fastest growing (fundamental) mode is indicated with a  $\times$  (+) symbol.

$f(z) \exp(-i\omega t + ikx)$  where  $\sigma = -\text{Im}(\omega)$  is the growth rate. The key differences between the present analysis and the one performed in [Kunz \(2011\)](#) are thus that *i*) we retain the  $z$ -dependence of all background variables instead of assuming locality in the vertical direction and *ii*) that we employ reflective boundary conditions at the top and bottom of the domain. More details on this type of analysis can be found in e.g. [Latter & Kunz \(2012\)](#); [Berlok & Pessah \(2016b\)](#) where configurations with a vertical magnetic field leading to the HBI were analyzed. The linearized equations for a background horizontal magnetic field are

$$-i\omega \frac{\delta \rho}{\rho} = -ik \delta v_x - \left( \frac{d \ln \rho}{dz} + \frac{\partial}{\partial z} \right) \delta v_z, \quad (\text{B1})$$

$$-i\omega \frac{\delta A}{B} = \delta v_z, \quad (\text{B2})$$

$$-i\omega \delta v_x = -ik \frac{\delta p}{\rho} + ik v_a^2 \frac{\partial \ln B}{\partial z} \frac{\delta A}{B} - v_{\parallel} \left( \frac{4}{3} k^2 \delta v_x + ik \frac{2}{3} \frac{\partial \delta v_z}{\partial z} \right), \quad (\text{B3})$$

$$-i\omega \delta v_z = -\frac{1}{\rho} \frac{\partial \delta p}{\partial z} - v_a^2 \left( k^2 + 2 \frac{\partial \ln B}{\partial z} \frac{\partial}{\partial z} + \frac{\partial^2}{\partial z^2} \right) \frac{\delta A}{B} - \frac{1}{\rho} \frac{\partial}{\partial z} \left( ik \rho v_{\parallel} \frac{2}{3} \delta v_x - \rho v_{\parallel} \frac{1}{3} \frac{\partial \delta v_z}{\partial z} \right), \quad (\text{B4})$$

$$-i\omega \frac{\delta T}{T} = -ik \frac{2}{3} \delta v_x - \left( \frac{d \ln T}{dz} + \frac{2}{3} \frac{\partial}{\partial z} \right) \delta v_z - \frac{2k^2 \chi_{\parallel} T}{3p} \left( \frac{\delta T}{T} + \frac{d \ln T}{dz} \frac{\delta A}{B} \right), \quad (\text{B5})$$

where  $\delta A$  is the perturbed vector potential and the perturbed magnetic field is obtained by computing  $\delta \mathbf{B} = \nabla \times (\delta A \mathbf{e}_y)$ . We solve the eigenvalue problem given by equations (B1)–(B5) with the aid of PSECAS ([Berlok & Pfrommer 2019](#)). In particular, we employ a Chebyshev-Gauss-Lobatto grid with the boundary condition that  $\delta \rho = \delta v_z = \delta A = 0$  at  $z = 0$  and  $z = H$ . The condition on the vector potential corresponds to enforcing a horizontal magnetic field at the boundaries.

We calculate the eigenmodes for an atmosphere with  $\beta_0 = 10^6$  and  $\text{Kn}_0^{-1} = 2000$  as a function of  $n = k_{\parallel}H/2\pi$ . For each  $n$ , a

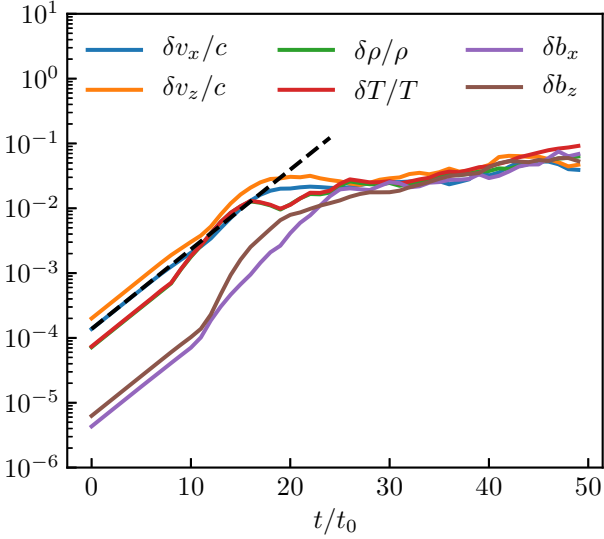


**Figure B3.** Exponential growth of the amplitude of perturbations in a MTI simulation with  $S_D = 0.01$  excited using the fundamental mode  $k_x = 2\pi/H$  with the fastest growth (i.e.  $n = 1, m = 0$ ). The dashed black line shows the theoretical growth.

set of solutions are obtained which are given an  $m$  mode number according to their growth rates (with  $m = 0$  the fastest,  $m = 1$  the second fastest, and so on). The  $\delta v_z$  component of a subset of the obtained solutions are shown in Fig. B1. The growth rates as function of  $n$  and  $m$  are shown in Fig. B2.

Due to the reflective boundary conditions, all modes have a vertical variation. It can be observed that the number of interior zero crossings is given by the  $m$  mode number. The modes with high  $n$  and low  $m$  are stratified with larger amplitude at the top of the domain. As  $m$  is increased, the modes penetrate deeper down into the atmosphere. The growth rates mainly depend on  $n$  (see Fig. B2). The variation in growth rate with  $m$  is not large and is consistent with the differences found when using local, linear theory to estimate the growth rate at the top ( $m = 0$ ) and bottom (for  $m > n$  the modes look sinusoidal in  $z$  and penetrate all the way down).

In local, linear theory the fastest growing mode has  $k_z = 0$  (see e.g. Kunz 2011). These are derived in the Boussinesq approximation where  $k_x \delta v_x + k_z \delta v_z = 0$ . The fastest growing mode therefore has  $\delta v_x = 0$  and a constant-with-height amplitude of  $\delta v_z$ . When using reflective boundary conditions, as in our quasi-global theory,  $\delta v_z$  is enforced to go to zero at the boundaries (see Fig. B1). As a consequence of this variation with  $z$ , the modes shown in Fig. B1 have  $\delta v_x \neq 0$  and a non-zero velocity divergence,  $\nabla \cdot \mathbf{v} \neq 0$ . The pressure anisotropy of a quasi-global eigenmode, given by  $\Delta p = \rho v_{\parallel} (2ik_x \delta v_x - \partial \delta v_z / \partial z)$ , is consequently linear in the amplitude of the velocity perturbations. For the fastest growing local mode (which has  $k_z = \delta v_x = 0$ ), the magnitude of the pressure anisotropy is given by  $\Delta p = 3\rho v_{\parallel} ik_x \delta v_z \delta b_z$ , i.e., its magnitude is only second order in the perturbation amplitude. For this reason, the magnitude of the pressure anisotropy in quasi-global modes is larger than for the fastest growing local mode.

A comparison between the linear growth rate found with PSE-CAS and the simulation presented in Fig. 2 is presented in Fig. B3. The exponential growth of perturbations follows the theoretical prediction until mirror-unstable regions interrupt the mode. Note that

**Table C1.** Overview of simulations presented in the main body of the paper. The left and right columns of Fig. 6 are abbreviated as 6L and 6R, respectively.

$\beta_0$	$\text{Kn}_0^{-1}$	Resolution	$S_D$	Figure
$10^6$	2000	$256 \times 256$	0.01	2, 3, B3
$10^7$	2000	$1024 \times 2048$	1, 0.01	6R
$10^6$	2000	$512 \times 1024$	1, 0.01	6R
$10^5$	2000	$512 \times 1024$	1, 0.2, 0.01	6R, 11
$10^4$	2000	$512 \times 1024$	1, 0.01	6R
$10^5$	20000	$256 \times 512$	1, 0.01	6L
$10^5$	2000	$256 \times 512$	1, 0.01	4, 5, 6L
$10^5$	200	$256 \times 512$	1, 0.01	6L
$10^5$	20	$256 \times 512$	1, 0.01	6L
$10^5$	2000	$256 \times 256 \times 512$	1, 0.01	8, 9, 10

the  $kH = 2\pi$  mode is not the fastest growing and that faster growing modes are excited when the interruption occurs (see Fig. B2).

### APPENDIX C: RESOLUTION STUDY

We perform a convergence study of the MTI simulations by considering three levels of uniform resolution, i.e.,  $N_x = 256, 512$  and  $1024$  with twice as many cells in the  $z$ -direction. We show maps of magnetic field strength in Fig. C1 and magnetic energy evolution in Fig. C2. First, we note that simulations with high  $\beta_0$  require higher spatial resolution in order to resolve thin magnetic field structures, see Fig. C1. This is the case regardless of whether  $S_D = 0.01$  (as in Fig. C1) or whether  $S_D = 1$ . When performing the parameter study in  $\beta_0$  at fixed  $\text{Kn}_0^{-1} = 2000$  (in Section 3.5, see the right-hand column of Fig. 6), we therefore use  $N_x = 1024$  for  $\beta_0 = 10^7$  and  $N_x = 512$  for the  $\beta_0 = 10^6, 10^5$  and  $10^4$  simulations. Second, we note that decreasing  $\text{Kn}_0^{-1}$  increases the computational cost of simulations due to the time step constraint imposed by the parabolic heat transport term. We are severely limited by the computational cost when  $\text{Kn}_0^{-1} = 20$ , and therefore perform the parameter study where we vary  $\text{Kn}_0^{-1}$  at fixed  $\beta_0 = 10^5$  with  $N_x = 256$  (in Section 3.5, see the left-hand column of Fig. 6). This resolution appears to be sufficient when  $\beta = 10^5$ , see Fig. C2, but would not be sufficient when  $\beta = 10^7$ .

We consider the evolution of the vertical magnetic energy in simulations with and without suppression of heat conductivity, numerical resolution  $N_x = 256, 512$  and  $1024$ , and initial magnetic field strength given by  $\beta_0 = 10^5$  and  $10^7$ , see Fig. C2. In the upper panel where  $\beta_0 = 10^5$ , the evolution of the energy remains qualitatively and quantitatively the same as the resolution is increased (with only a very minor systematic increase in the energy of the final state with resolution). The initial amplitude of the MTI seeding decreases with resolution (because dissipation of the Gaussian noise by viscosity is more efficient at high resolution). We have adjusted the starting time of the  $N_x = 512$  and  $1024$  simulations accordingly. The  $\beta_0 = 10^7$  simulations are not as well converged. Qualitatively, however, the saturation energy of the  $S_D = 0.01$  simulation is always slightly lower than in the  $S_D = 1$  reference simulation. This can be understood from the sustained presence of mirror-unstable regions in simulations with  $\beta_0 = 10^7$  and  $\text{Kn}_0^{-1} = 2000$  (see Fig. 6).

We summarize the resolutions used in the simulations presented in the main body of the paper in Table C1 and the convergence tests in Table C2.



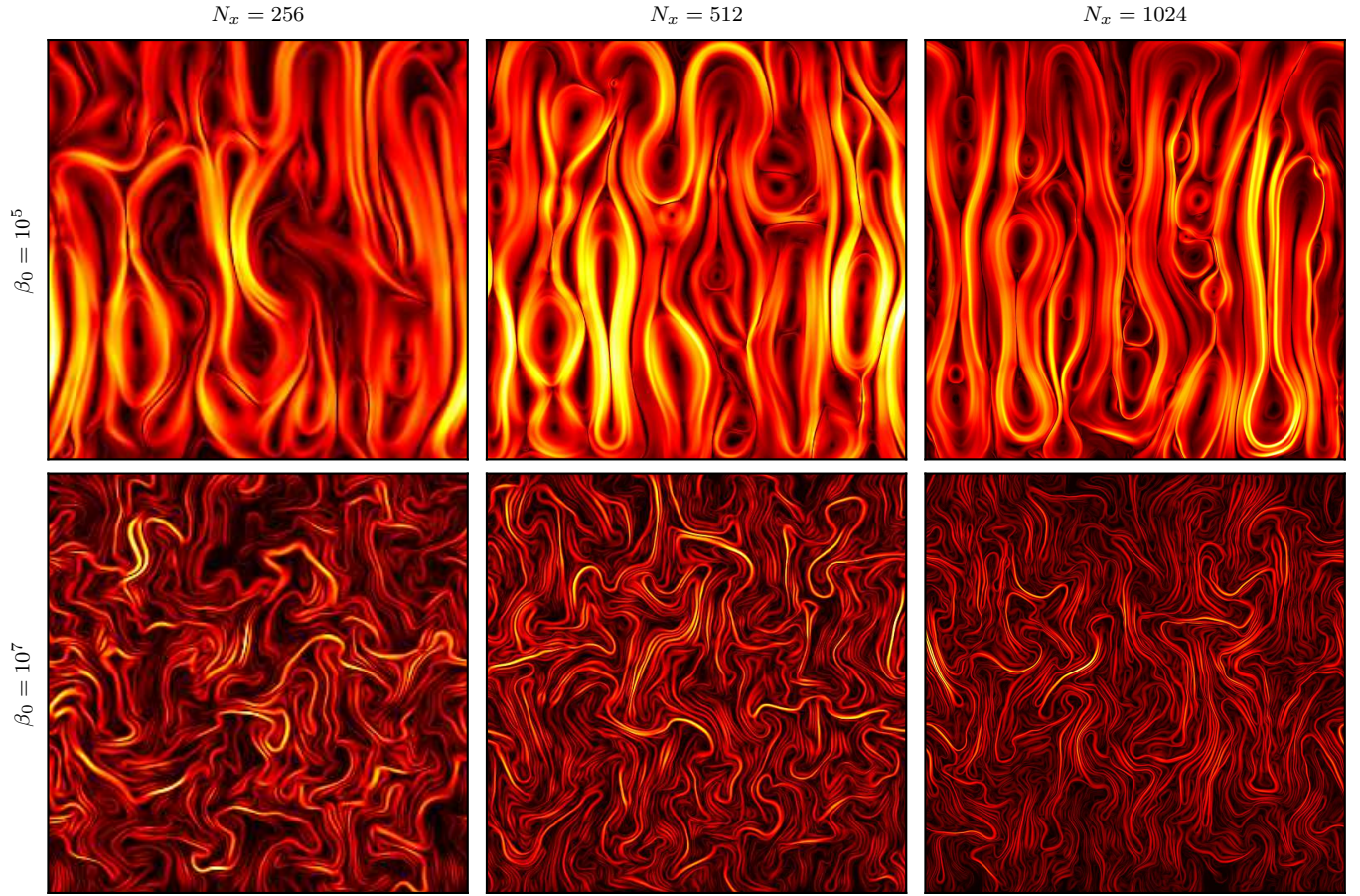


**Figure C1.** Magnetic field strength,  $|B|$ , at  $t/t_0 = 50$  in 6 different simulations. A very high spatial resolution is required to resolve the thin magnetic field structures that arise in simulations in which the magnetic field is weak. The central, unstable part of the simulation domain is shown.

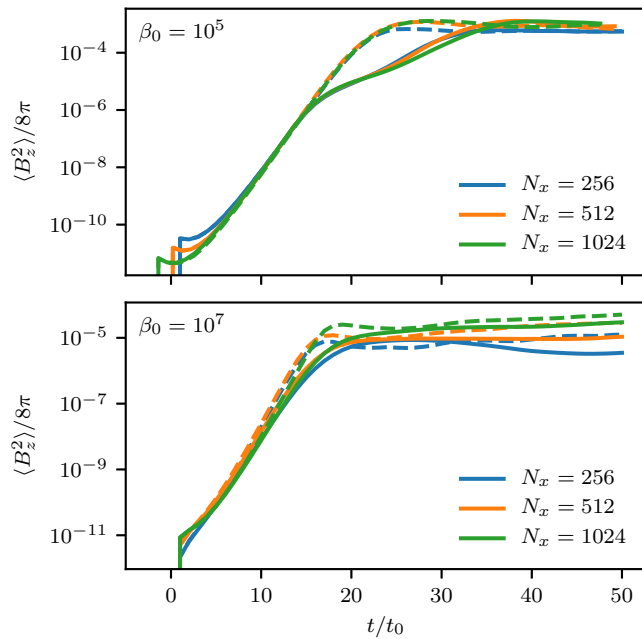


**Figure C2.** Convergence test of MTI simulations with  $\beta = 10^5$  (upper panel) and  $\beta = 10^7$  (lower panel). Simulations with  $S_D = 0.01$  ( $S_D = 1$ ) shown with solid (dashed) lines.

**Table C2.** Overview of convergence tests. The lowest resolution was  $128 \times 256$  in 2D ( $128 \times 128 \times 256$  in 3D) and the highest numerical resolution performed is stated in the table. All intermediate resolutions (i.e. powers of two) were also performed.

$\beta_0$	$\text{Kn}_0^{-1}$	Resolution	$S_D$
$10^7$	2000	$1024 \times 2048$	1, 0.01
$10^6$	2000	$1024 \times 2048$	1
$10^6$	2000	$512 \times 1024$	0.01
$10^5$	2000	$1024 \times 2048$	1, 0.01
$10^4$	2000	$1024 \times 2048$	1
$10^4$	2000	$512 \times 1024$	0.01
$10^5$	20000	$256 \times 512$	1, 0.01
$10^5$	200	$256 \times 512$	1, 0.01
$10^5$	20	$256 \times 512$	1, 0.01
$10^5$	2000	$256 \times 256 \times 512$	1, 0.01